

RELATIVISTIC JET FORMATION FROM BLACK HOLE MAGNETIZED ACCRETION DISKS: METHOD, TESTS, AND APPLICATIONS OF A GENERAL RELATIVISTIC MAGNETOHYDRODYNAMIC NUMERICAL CODE

SHINJI KOIDE

Faculty of Engineering, Toyama University, Gofuku, Toyama 930-8555, Japan

AND

KAZUNARI SHIBATA¹ AND TAKAHIRO KUDOH

National Astronomical Observatory, Mitaka, Tokyo 181-8588, Japan

Received 1998 September 9; accepted 1999 February 17

ABSTRACT

Relativistic jets are observed in both active galactic nuclei (AGNs) and “microquasars” in our Galaxy. It is believed that these relativistic jets are ejected from the vicinity of black holes. To investigate the formation mechanism of these jets, we have developed a new general relativistic magnetohydrodynamic (GRMHD) code. We report on the basic methods and test calculations to check whether the code reproduces some analytical solutions, such as a standing shock and a Keplerian disk with a steady state infalling corona or with a corona in hydrostatic equilibrium. We then apply the code to the formation of relativistic MHD jets, investigating the dynamics of an accretion disk initially threaded by a uniform poloidal magnetic field in a nonrotating corona (either in a steady state infall or in hydrostatic equilibrium) around a nonrotating black hole. The numerical results show the following: as time goes on, the disk loses angular momentum as a result of magnetic braking and falls into the black hole. The infalling motion of the disk, which is faster than in the nonrelativistic case because of general relativistic effects below $3r_s$ (r_s is the Schwarzschild radius), is strongly decelerated around $r = 2r_s$ by centrifugal force to form a shock inside the disk. The magnetic field is tightly twisted by the differential rotation, and plasma in the shocked region of the disk is accelerated by the $\mathbf{J} \times \mathbf{B}$ force to form bipolar relativistic jets. In addition, and interior to, this *magnetically driven jet*, we also found a *gas-pressure-driven jet* ejected from the shocked region by the gas-pressure force. This *two-layered jet structure* is formed not only in the hydrostatic corona case but also in the steady state falling corona case.

Subject headings: accretion, accretion disks — black hole physics — galaxies: jets — MHD — relativity

1. INTRODUCTION

Knots from many active galactic nuclei (AGNs) sometimes propagate with apparent velocities exceeding the speed of light (Pearson et al. 1981; Hughes 1991). This phenomenon, called superluminal motion, is thought to be due to a relativistic jet with Lorentz factor 2–20 propagating almost directly along the line of sight (Rees 1966). Since the velocity of the jet is highly relativistic, the jet is believed to be accelerated in the vicinity of a supermassive black hole that is located in the center of the AGN. Recently, X-ray and radio observations have revealed compelling evidence of the existence of black holes (Tanaka et al. 1995; Miyoshi et al. 1995). Superluminal motion has been observed from “microquasars” GRS 1915+105 and GRO J1655–40 in our Galaxy (Mirabel & Rodriguez 1994; Tingay et al. 1995). In spite of the vast difference in the luminosity and the size of the microquasars in our Galaxy and those of AGNs, both are believed to be powered by gravitational energy released during accretion of plasma onto black holes (Lynden-Bell 1969; Rees 1984).

One of the most promising models for jet formation is the magnetic acceleration model (Blandford & Payne 1982). This mechanism has been proposed not only for AGN jets (e.g., Lovelace 1976; Matsumoto et al. 1996; Pelletier et al. 1996; Meier et al. 1997) but also for protostellar jets (e.g., Pudritz & Norman 1986; Uchida & Shibata 1985; Shibata

& Uchida 1986; Ouyed, Pudritz, & Stone 1997). According to a recent study of magnetically driven jets by Kudoh & Shibata (1995, 1997a, 1997b; Kudoh, Matsumoto, & Shibata 1998), the terminal velocity of a jet is comparable to the rotational velocity of the disk at the foot of the jet. Therefore, to produce a relativistic jet, the foot should be near the event horizon of a black hole. Recently, the X-ray $K\alpha$ lines from the inner regions of an accretion disk around a supermassive black hole in an AGN have been observed (Bromley, Miller, & Pariev 1998). The observations show that this inner edge of the iron $K\alpha$ line emission region is within 2.6 ± 0.3 times the Schwarzschild radius $r_s \equiv 2GM_{\text{BH}}/c^2$ —the event horizon of a nonrotating black hole (G is the gravitational constant, and M_{BH} is the mass of the central black hole). The inner region may be related to the jet itself. In fact, observations show evidence of a disk-jet interaction in the microquasar GRS 1915+105 (Eikenberry et al. 1998). In the region, the plasma and the magnetic field interact with each other in a complicated manner in the general relativistic framework, so that a general relativistic magnetohydrodynamic (GRMHD) treatment is needed.

Analytic models of relativistic stationary flows from black holes and pulsar magnetospheres have been developed (see review by Beskin 1997) under the assumption of fixed poloidal magnetic field (Camenzind 1986; Takahashi et al. 1990; Takahashi & Shibata 1998), force-free magnetic field (Okamoto 1992), self-similar solutions (Li, Chiueh, & Begelman 1992), or asymptotic solutions (Begelman & Li 1994; Tomimatsu 1994). To study the nonsteady properties

¹ Present address: Kwasan and Hida Observatories, Kyoto University, Yamashima, Kyoto 607-8471, Japan.

of jets propagating through magnetized plasmas, several authors have performed numerical simulations using special relativistic MHD codes (Koide, Nishikawa, & Mutel 1996; van Putten 1996; Koide 1997; Nishikawa et al. 1997, 1998). In the general relativistic regime, Hawley & Smarr (1985) carried out (nonmagnetic) hydrodynamic simulations of jet formation near a black hole, while Yokosawa (1993) performed general relativistic MHD simulations of accretion onto a rotating black hole. However, no one has yet performed full GRMHD numerical simulations of the formation of jets in a vicinity of a black hole except for a brief paper by Koide, Shibata, & Kudoh (1998). In that paper, the black hole is assumed initially to have a hot corona in hydrostatic equilibrium around it, with a cold Keplerian disk embedded inside the corona. The Keplerian disk is threaded by a uniform poloidal magnetic field initially. The numerical results show that a relativistic jet is formed with a two-layered shell structure. The inner jet is fast and accelerated by high gas pressure resulting from a strong collision between the infalling disk gas and the disk gas stagnated by the centrifugal barrier and/or the high-density region of the hydrostatic corona near the horizon. The outer jet is slow and accelerated by the magnetic field as shown in nonrelativistic MHD simulations (Uchida & Shibata 1985; Shibata & Uchida 1986; Kudoh & Shibata 1995, 1997a, 1997b).

In this paper, we present the basic methods, test runs, and applications of the full GRMHD numerical simulations. The applications contain the first calculation of a relativistic jet formation in a free-falling corona around a black hole surrounded by the accretion disk. We have developed a GRMHD code using the simplified total variation diminishing (TVD) method. The method is able to resolve the structure and evolution of the accretion flow near the horizon and the production of the jet.

In the next section, the basic methods of the simulation are presented. In § 3, we report on the test runs of the code. In §§ 4 and 5, the applications to the formation of MHD jets in the vicinity of the black hole are shown. In the last section, the discussion and summary are presented.

2. NUMERICAL METHODS

2.1. Basic Equations

Our study is based on the general relativistic conservation laws of mass, momentum, and energy of single-component conductive fluids and on Maxwell equations (Weinberg 1972; Thorne, Price, & Macdonald 1986),

$$\nabla_\nu(\rho U^\nu) = 0, \quad (1)$$

$$\nabla_\nu T_g^{\mu\nu} = 0, \quad (2)$$

$$\partial_\mu F_{\nu\lambda} + \partial_\nu F_{\lambda\mu} + \partial_\lambda F_{\mu\nu} = 0, \quad (3)$$

$$\nabla_\mu F^{\mu\nu} = -J^\nu, \quad (4)$$

where U^ν and J^ν are four-velocity and four-current density, respectively. Scalar values ρ , p , and e are proper mass density, proper pressure, and proper total energy density $e \equiv \rho c^2 + p/(\Gamma - 1)$, respectively. Here Γ is the specific-heat ratio; ∇_μ is covariant derivative; and the general relativistic energy momentum tensor $T_g^{\mu\nu}$ is given by

$$T_g^{\mu\nu} = pg^{\mu\nu} + (e + p)U^\mu U^\nu + F^\mu_\sigma F^{\nu\sigma} - g^{\mu\nu} F^{\lambda\kappa} F_{\lambda\kappa}/4, \quad (5)$$

where $g^{\mu\nu}$ is metric, $F^{\mu\nu}$ is the electromagnetic field-strength tensor, $F_{\mu\nu} = \partial_\mu A_\nu - \partial_\nu A_\mu$, and A^μ is four-vector potential. We assume that the off-diagonal elements of the metric $g_{\mu\nu}$

vanish,

$$g_{\mu\nu} = 0 \quad (\mu \neq \nu), \quad (6)$$

and we put

$$h_0 = \sqrt{-g_{00}}, \quad h_1 = \sqrt{g_{11}}, \quad h_2 = \sqrt{g_{22}}, \quad h_3 = \sqrt{g_{33}}. \quad (7)$$

To perform the simulations, we use the 3 + 1 form of these equations (see Appendix A). With the assumption of a diagonal metric, the equations reduce to the familiar form of special relativistic magnetohydrodynamics (Koide et al. 1996; Koide 1997) with general coordinates, plus the addition of gravitational terms and a scale factor h_0 . In these equations, the velocity of light c is written explicitly, so that when we take the nonrelativistic limit of these equations ($c \rightarrow \infty$), they reduce to standard Newtonian magnetohydrodynamics. We call these the general relativistic MHD (GRMHD) equations. We assume the infinite electric conductivity condition,

$$F_{\nu\mu} U^\nu = 0. \quad (8)$$

Using this condition, the equations (1)–(3) close self-consistently. Vectors such as velocity \mathbf{v} and magnetic field \mathbf{B} are defined in the local frame (see Appendix A for an explicit expression). Equation (4) is used to calculate the electric charge density ρ_c and current density \mathbf{J} (see Appendix A). For the case of resistive MHD flow in a black hole magnetosphere, the reader is referred to the analytic models presented by Kudoh (1994), Kudoh & Kaburaki (1996), and Khanna (1998).

2.2. Numerical Scheme

We have developed a three-dimensional GRMHD numerical code that employs the *simplified total variation diminishing* (TVD) method (see Appendix D), which was developed by Davis (1984) for violent phenomena such as shocks. This method is similar to Lax-Wendroff's method with the addition of a diffusion term formally. In order to integrate the time-dependent conservation laws, we need only the maximum speed of waves and not each eigenvector or eigenvalue of the Jacobian.

We tested this method using special relativistic simulations of sound and magnetosonic shock waves, checking the energy conservation law and its propagation properties. Furthermore, we confirmed that, in the nonrelativistic limit, the code gives the same results on calculations of the Kelvin-Helmholtz instability and magnetized jet production as a standard Newtonian (nonrelativistic) MHD code. Note that in the GRMHD simulations we have to check not only Gauss's law for the magnetic field, $\nabla \cdot \mathbf{B} = 0$, but also the charge conservation law, $\partial \rho_c / \partial t + \nabla \cdot \mathbf{J} = 0$, where ρ_c and $\mathbf{J} \equiv (J_1, J_2, J_3)$ are charge density and current density calculated by equation (4) with four current density $J^\mu = (ch_0^{-2}\rho_c, (h_0 h_i)^{-1}J_i)$, $i = 1, 2, 3$ (see Appendix A). In our calculation, the conservation law is satisfied quite well, within very small error of order $10^{-5} B_0/L^2$. (B_0 and L are the characteristic magnetic field strength and length, respectively. For example, the characteristic length L is r_s in the general relativistic case.)

With the simplified TVD method, we obtain only the conserved quantities D , \mathbf{P} , ϵ , and \mathbf{B} directly at each step from the difference equations. In the next step, we must calculate \mathbf{v} and p from D , \mathbf{P} , ϵ , and \mathbf{B} from equations (A4), (A5), and (A6) in Appendix A. To do this, we solve two nonlinear, simultaneous algebraic equations with unknown

variables $x \equiv \gamma - 1$ and $y \equiv \gamma(\mathbf{v} \cdot \mathbf{B})/c^2$,

$$x(x+2) \left[\Gamma a x^2 + (2\Gamma a - b)x + \Gamma a - b + d + \frac{\Gamma}{2} y^2 \right]^2 \\ = (\Gamma x^2 + 2\Gamma x + 1)^2 [\tau^2(x+1)^2 + 2\sigma y + 2\sigma x y + \beta^2 y^2], \quad (9)$$

$$\left[\Gamma(a - \beta^2)x^2 + (2\Gamma a - 2\Gamma\beta^2 - b)x + \Gamma a - b + d - \beta^2 + \frac{\Gamma}{2} y^2 \right] y = \sigma(x+1)(\Gamma x^2 + 2\Gamma x + 1), \quad (10)$$

where $a = D + \epsilon/c^2$, $b = (\Gamma - 1)D$, $d = (1 - \Gamma/2)B^2/c^2$, $\tau = P/c$, $\beta = B/c$, and $\sigma = \mathbf{B} \cdot \mathbf{P}/c^2$. Note that in the absence of the magnetic field equation (9) becomes the equation in the relativistic hydrodynamic case, as derived by Duncan & Hughes (1994), and equation (10) becomes a trivial equation. The equations are solved at each cell using a two-variable Newton-Raphson iteration method. We then easily calculate p and \mathbf{v} using x , y , D , \mathbf{P} , ϵ , and \mathbf{B} . This method is identical to that in the special relativistic case (Koide et al. 1996; Koide 1997).

2.3. Metric and Coordinates

The Schwarzschild metric, which describes the spacetime around the black hole at rest, is used in the calculation as $h_0 = \alpha$, $h_1 = 1/\alpha$, $h_2 = r$, $h_3 = r \sin \theta$ where α is the lapse function, $\alpha \equiv (1 - r_s/r)^{1/2}$, and r is the radial coordinate in the Boyer-Lindquist set (ct, r, θ, ϕ) . However, we actually use the modified *tortoise* radial coordinate, $x = \ln(r/r_s - 1)$. With a uniform mesh in this coordinate, along with the azimuthal ϕ and polar coordinates θ , the radial mesh width of the Boyer-Lindquist coordinates is proportional to $r - r_s$. Since the eigenspeed of the MHD waves near the black hole is very small because of the lapse function α , the CFL numerical stability condition is not severe near the black hole where the mesh width is smallest. Rather, it is most severe near $r = 1.5r_s$. This indicates that these modified *tortoise* coordinates are appropriate for the calculation both near and far from the black hole.

3. TEST OF THE CODE

3.1. Transonic Solutions

We first shall discuss tests of the GRMHD code. The first test checks the steady state infall of a finite pressure gas into the black hole (Bondi & Hoyle 1944). This flow is approximately in free fall, and we refer to it as *free fall* below. We assume spherical symmetry and a polytropic equation of state $p \propto \rho^\Gamma$. The equation of the motion of the finite gas can be integrated to give

$$F = \left(\frac{H}{\alpha\gamma} - 1 \right) \left(\alpha r^2 \gamma \frac{v}{c} \right)^{\Gamma-1}, \quad (11)$$

where F (a kind of adiabatic invariant) and H (\sim specific enthalpy) are constants of the motion and α and γ are the lapse function and Lorentz factor. Here H and F are written as

$$H = \alpha_0 \gamma_0 \left(1 + \frac{\Gamma}{\Gamma-1} \frac{p_0}{\rho_0 c^2} \right), \quad (12)$$

$$F = \frac{\Gamma}{\Gamma-1} \frac{p_0}{\rho_0 c^2} \left(\alpha_0 r_0^2 \gamma_0 \frac{v_0}{c} \right)^{\Gamma-1}, \quad (13)$$

with the values α_0 , γ_0 , p_0 , ρ_0 , and v_0 evaluated at an arbitrary point $r = r_0$. Figure 1a shows the contour map of F

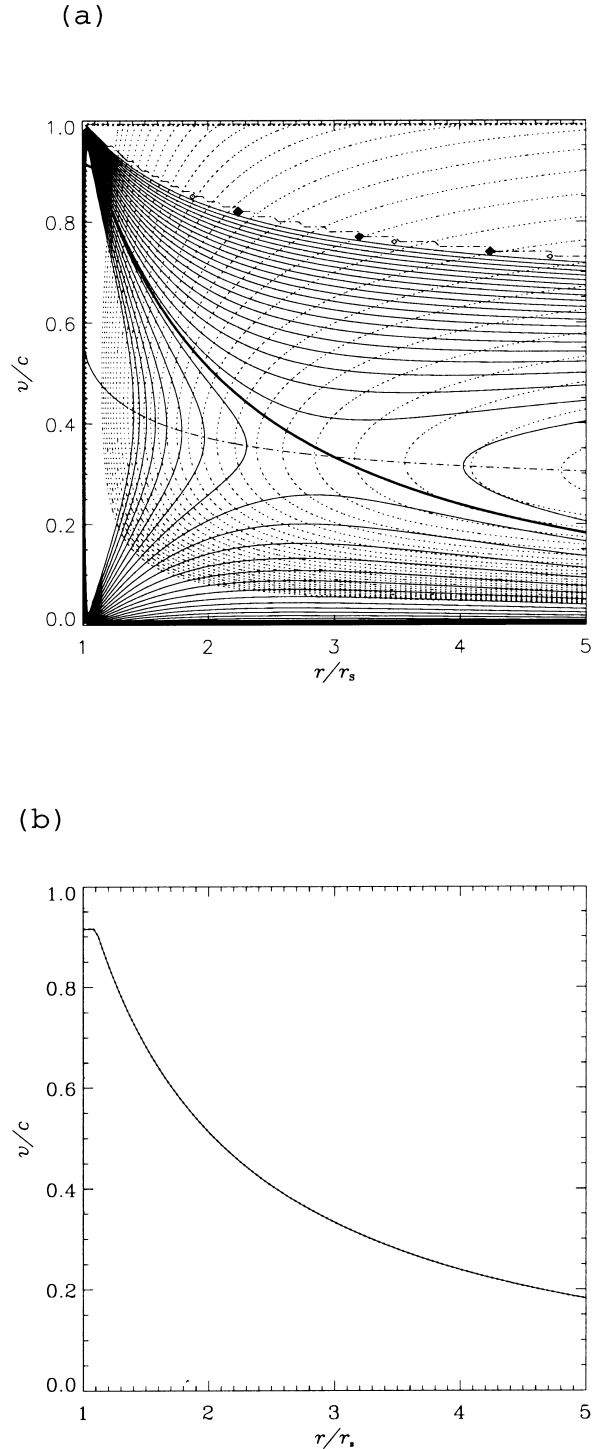


FIG. 1.—Initial conditions and simulation results of a transonic solution with $\Gamma = 4/3$ and $H = 1.3$. (a) Transonic solution (thick solid line), solutions for finite pressure gas (thin solid lines), and sonic point (dash-dotted line). The dotted lines show the contour map of P/Qc^2 (see § 3.2). (b) Initial accretion velocity (dotted line) and simulation results at $t = 1\tau_s$ (solid line). They are in good agreement with each other, which shows the validity of the simplified TVD GRMHD code.

(thin solid lines) when $H = 1.3$ and $\Gamma = 4/3$. Each contour line gives the velocity distribution of the steady state gas flow. The thick solid line indicates the transonic solution, which passes through the sonic point from the subsonic to supersonic region. Let us write the transonic flow velocity, density, and pressure by $v = v_{\text{ffc}}$, $\rho = \rho_{\text{ffc}}$, and $p = p_{\text{ffc}}$,

respectively. The sonic point is given by the condition,

$$\frac{\partial F}{\partial \gamma} = 0, \quad \frac{\partial F}{\partial \alpha} = 0, \quad (14)$$

for a given H and Γ . The former equation $\partial F/\partial \gamma = 0$ (Fig. 1a, dash-dotted line) gives the sonic flow condition $v = v_s \equiv (\Gamma p/h)^{1/2} c$, where h is the relativistic enthalpy, $h \equiv \rho c^2 + \Gamma p/(\Gamma - 1)$. Therefore the upper and lower regions of the dash-dotted line correspond to the super- and/or subsonic flow, respectively. The simultaneous equations (14) reduce to

$$(H^2 - 1)x^3 + \left(\frac{9}{4} - 2gH^2\right)x^2 + \left(H^2g^2 - \frac{3^3}{4^2}\right)x + \left(\frac{3}{4}\right)^3 = 0, \quad (15)$$

where $x \equiv r/r_s$, $g \equiv (3\Gamma - 2)/4(\Gamma - 1)$. The velocity at $r = xr_s$ is determined by $v = v_s$, which is given by

$$\alpha = \frac{H(\gamma^{-2} + \Gamma - 2)}{(\Gamma - 1)\gamma}. \quad (16)$$

In Figure 1a, the sonic point of the transonic solution is located at $r = 3r_s$. (The dotted lines show the contour of the specific momentum.) Figure 1b shows the time evolution of the transonic solution calculated by the simplified TVD method in the region $1.1r_s \leq r \leq 20r_s$. We use 300 mesh points along the radial coordinate. In this test case, the mesh spacings at $r = 1.1r_s$ and $r = 20r_s$ are $1.7 \times 10^{-3}r_s$ and $0.35r_s$, respectively. The solid line shows the infall velocity at $t = 1\tau_s$, and the dashed line shows the initial velocity. These lines are identical with each other, showing that the simplified TVD method reproduces the transonic solution quite well.

3.2. Transonic Solution with a Shock

Next we performed a calculation of transonic infall with a shock. The parameters, Γ and H are the same as those in the above situation: $\Gamma = 4/3$ and $H = 1.3$. We considered the case where a standing shock is located at $r = 4r_s \equiv r_{\text{shock}}$. The Rankine-Hugoniot conditions at the shock front normally are given by the equations for conservation of mass $Q \equiv \rho \gamma u$, specific enthalpy $H/\alpha = \gamma h/\rho c^2$, and total pressure $P \equiv hu^2 + p$, where u is four-velocity, $u \equiv \gamma v/c$. However, in our test we use the continuity condition on P/Qc^2 instead of the last condition on the total pressure P . Here we consider only the flow with $H = 1.3$ so that the second continuity condition on H/α is automatically satisfied. The proper mass density ρ is determined to satisfy the first continuity condition about Q , independent of the condition of H/α and P/Qc^2 . This is because the latter conditions contain ρ only as the ratio with other quantities such as p . Therefore, it is enough to take care of only the last continuity condition of P/Qc^2 . Figure 2a shows the contour map of F (thin solid lines) and P/Qc^2 (dotted lines). The down-stream condition is given by the transonic solution described in § 3.1 without the shock. The up-stream condition at the shock front is determined by the Rankine-Hugoniot relation:

$$\frac{P_2}{Q_2 c^2} = \frac{P_1}{Q_1 c^2} = \frac{1}{u_1} \left[\frac{H}{\alpha} \frac{u_1^2}{\gamma_1} + \frac{\Gamma - 1}{\Gamma} \left(\frac{H}{\alpha \gamma_1} - 1 \right) \right] \quad (17)$$

where subscripts 1 and 2 denote the up-stream and down-stream quantities, respectively. The up-stream flow is calcu-

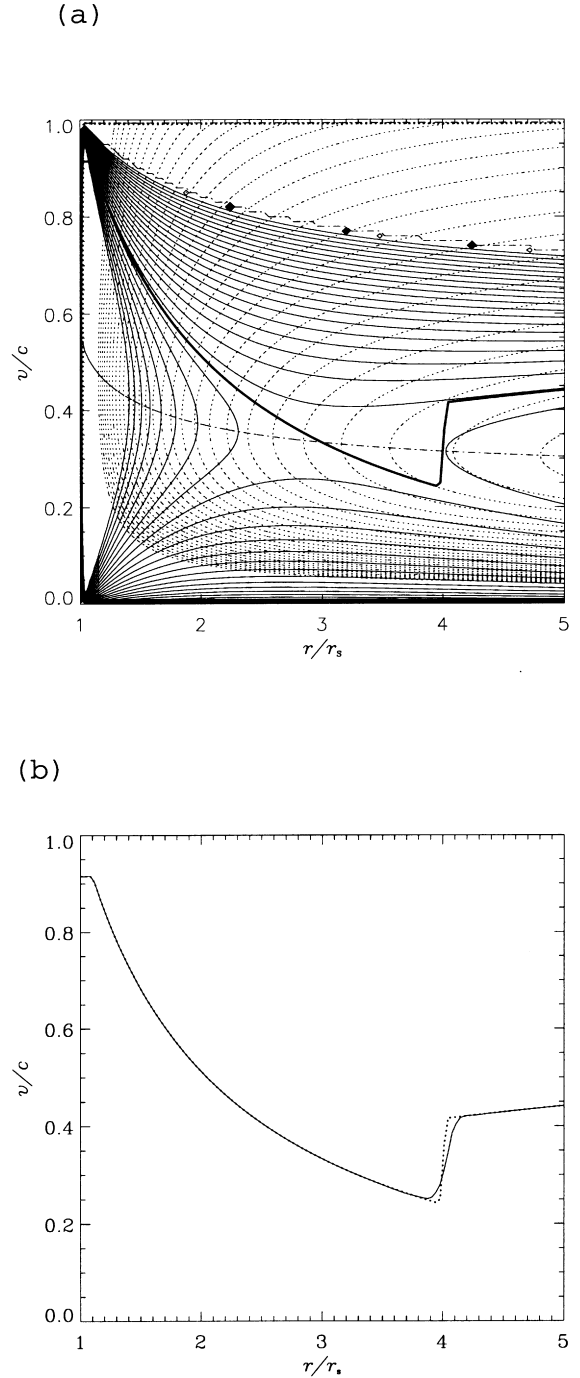


FIG. 2.—Initial conditions and simulation results of a transonic solution with a shock wave at $r = 4r_s$. Here $\Gamma = 4/3$ and $H = 1.3$. (a) Transonic solution with a standing shock wave at $r = 4r_s$ (thick solid line), solutions for finite pressure gas (thin solid lines), and sonic point (dash-dotted line). At the shock front, the up-stream and down-stream conditions have the same values of P/Qc^2 , which are shown by the contour map of dotted lines. (b) Initial accretion velocity (dotted lines) and simulation results at $t = 1\tau_s$ (solid lines). The velocity jump at the shock front is smoothed out slightly owing to the simplified TVD scheme. However, the other part is calculated perfectly. On the whole, the transonic solution with the shock is calculated properly by our code.

lated by the free-fall gas equation (11). Note that the condition $\partial(P/Qc^2)/\partial \gamma = 0$ provides the $v = v_s$ (sonic point). Therefore, the transition due to the shock should cross the sonic point ($v = v_s$).

Figure 2b shows the initial velocity (dashed line) and the velocity at $t = 1\tau_s$ (solid line), which is calculated by the

simplified TVD scheme. It shows that the shock is smeared a little numerically. However, on the whole, the transonic solution with a shock is calculated stably by the code.

3.3. Keplerian Motion in a Free-Fall Corona

Here we check the relativistic Keplerian motion in a transonic free-fall corona around a Schwarzschild black hole. The initial state of the corona is given by the transonic solution without a shock (see § 3.1), and the sonic point is located at $r = 1.6r_s$ for $\Gamma = 5/3$ and $H = 1.3$. We initialize the Keplerian disk in the corona as follows. The disk is located in the region $r > r_D \equiv 3r_s, |\cot \theta| < \delta = 1/8$. In this region, the density is 100 times that of the background corona (Fig. 3c), the azimuthal component of the velocity is the relativistic Keplerian velocity $v_\phi = v_K \equiv c/[2(r/r_s - 1)]^{1/2}$, and its poloidal component vanishes (Fig. 3a). (Note that this equation reduces to the Newtonian

Keplerian velocity $v_\phi = (GM/r)^{1/2}$ when the nonrelativistic limit $r_s/r \ll 1$ is taken.) The pressure of the corona and the disk are assumed to be equal to that of the transonic solution. The initial conditions of the whole plasma around the black hole are given as

$$\rho = \rho_{\text{ffc}} + \rho_{\text{dis}} \quad (18)$$

$$\rho_{\text{dis}} = \begin{cases} 100\rho_{\text{ffc}} & \text{if } r > r_D \text{ and } |\cot \theta| < \delta, \\ 0 & \text{if } r \leq r_D \text{ or } |\cot \theta| \geq \delta, \end{cases} \quad (19)$$

$$(v_r, v_\theta, v_\phi) = \begin{cases} (0, 0, v_K) & \text{if } r > r_D \text{ and } |\cot \theta| < \delta, \\ (-v_{\text{ffc}}, 0, 0) & \text{if } r \leq r_D \text{ or } |\cot \theta| \geq \delta, \end{cases} \quad (20)$$

$$p = p_{\text{ffc}}, \quad (21)$$

where we set $\delta = 0.125$. The smoothing length is $0.3r_s$. At $t = 10\tau_s$, the inner edge of the disk falls slightly inward

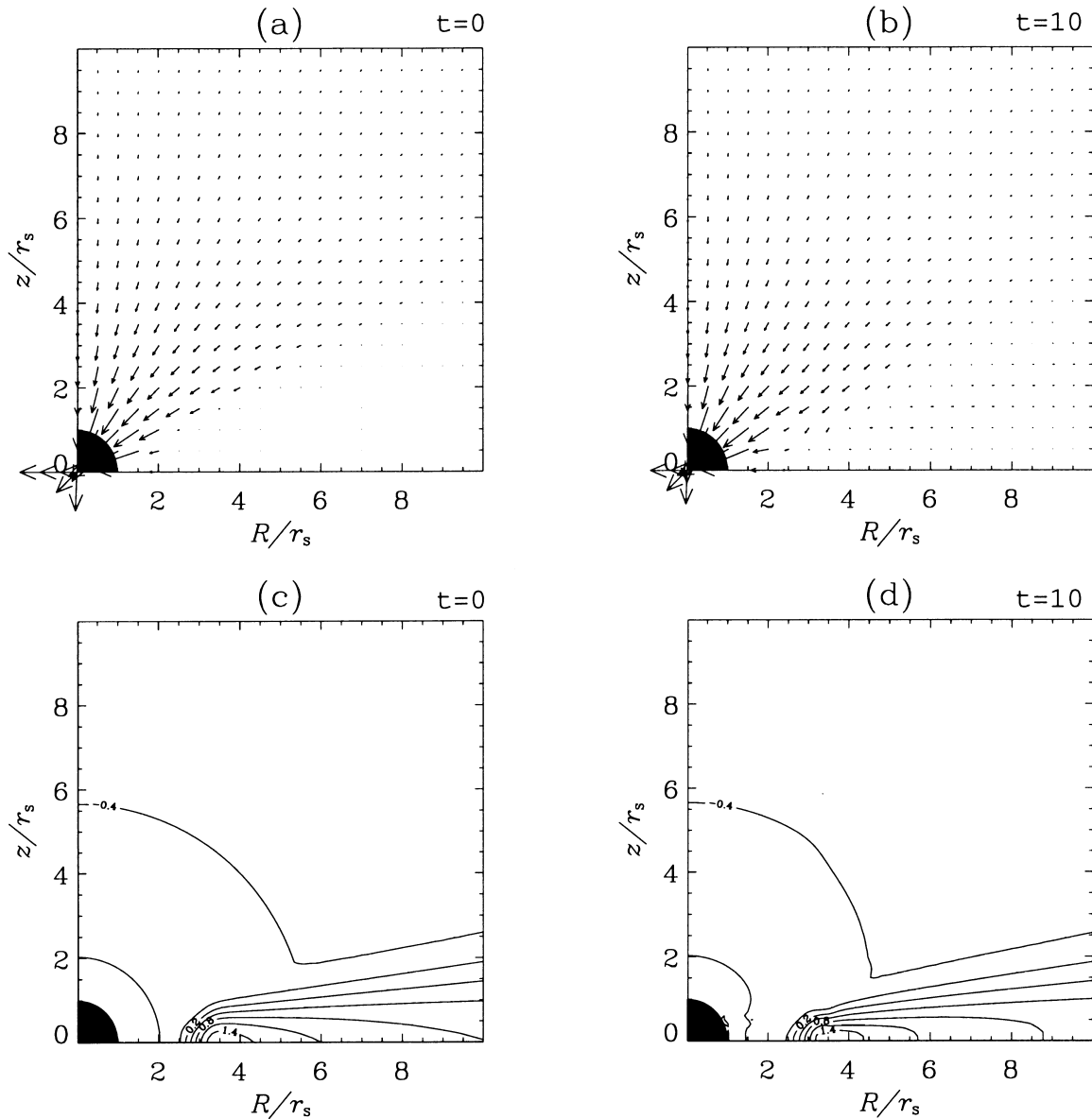


FIG. 3.—Results of Keplerian disk motion in a free-fall (steady state falling) corona (transonic solution). The conditions of the transonic solution are $\Gamma = 4/3, H = 1.3$. The density of the Keplerian disk is 100 times that of the corona. Black region shows the black hole. (a) The poloidal velocity in the initial condition. (b) The poloidal velocity at $t = 10\tau_s$. (c) The proper mass density in the initial condition. (d) The proper mass density at $t = 10\tau_s$. The Keplerian disk is stable, as expected.

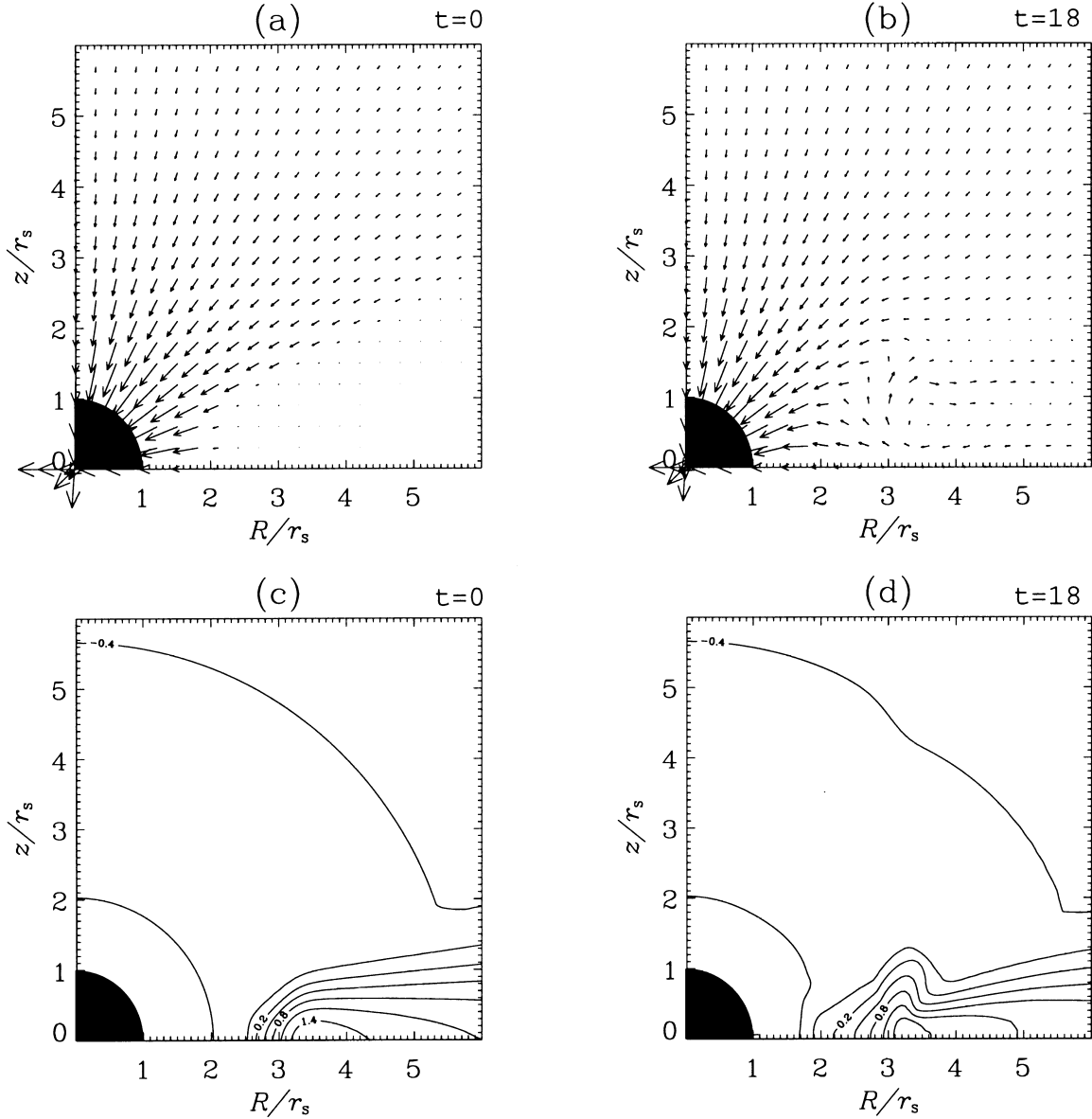


FIG. 4.—Results of sub-Keplerian disk motion in a free-fall (steady state falling) corona (transonic solution). The conditions of the transonic solution are $\Gamma = 4/3$ and $H = 1.3$. The azimuthal velocity of the disk is 80% of the Keplerian velocity. The density of the sub-Keplerian disk is 100 times that of the corona. Black region shows the black hole. (a) The poloidal velocity in the initial condition. (b) The poloidal velocity at $t = 18\tau_s$. (c) The proper mass density in the initial condition. (d) The proper mass density at $t = 18\tau_s$. We can see the deceleration of the fall of the disk around $r = 3r_s$. The high-density region is limited at $r \geq 2r_s$.

numerically (Figs. 3b and 3d). However, on the whole, the disk rotates stably and the transonic corona is also steady.

3.4. Sub-Keplerian Motion in a Free-Fall Corona

We also performed a simulation with a sub-Keplerian disk in a transonic free-fall corona. The initial condition is the same as that of the previous Keplerian disk case (Figs. 4a and 4c) except for the azimuthal velocity, which is 80% of the Keplerian velocity, $v_\phi = 0.8v_K$ in the disk. Initially, the disk begins to fall toward the black hole, but the flow stops around $r \sim 3r_s$, $z \sim 0$ at $t = 18\tau_s$ (Fig. 4b), with a high-density disk region forming at that point (Fig. 4d). This drastic deceleration is due to a centrifugal barrier. The energy conservation equation for the accretion of the test particle is

$$K + V = E, \quad (22)$$

where K corresponds to the *general relativistic kinetic energy* of the motion projected onto the radial coordinate, $K \equiv \log(1 - v_1^2/c^2)^{-1/2}$, V is the effective potential, $V \equiv \log[\alpha(1 + l^2/r^2)^{1/2}]$, and E is the *general relativistic total energy*. Here l is the normalized angular momentum $l \equiv r\gamma v_\phi/c$. The critical point is determined by $\partial V/\partial r = 0$, which yields a function of l , $r(l) = [l^2 - l(l^2 - 3r_s^2)^{1/2}]/r_s$. With respect to the negative energy motion ($E < 0$), the location of the critical point is restricted to $2r_s \leq r(l) \leq 3r_s$, where the equal signs occur when $l = 2r_s$ and $l = \sqrt{3}r_s$, respectively. This point corresponds to the watershed of the accretion flow, which is never seen in nonrelativistic cases. Above the watershed, the flow is stopped or decelerated by centrifugal force. On the other hand, below the watershed, the large gradient of the effective potential accelerates the material very rapidly toward the black hole horizon, where the infall velocity becomes the speed of light c (see Fig. 4b).

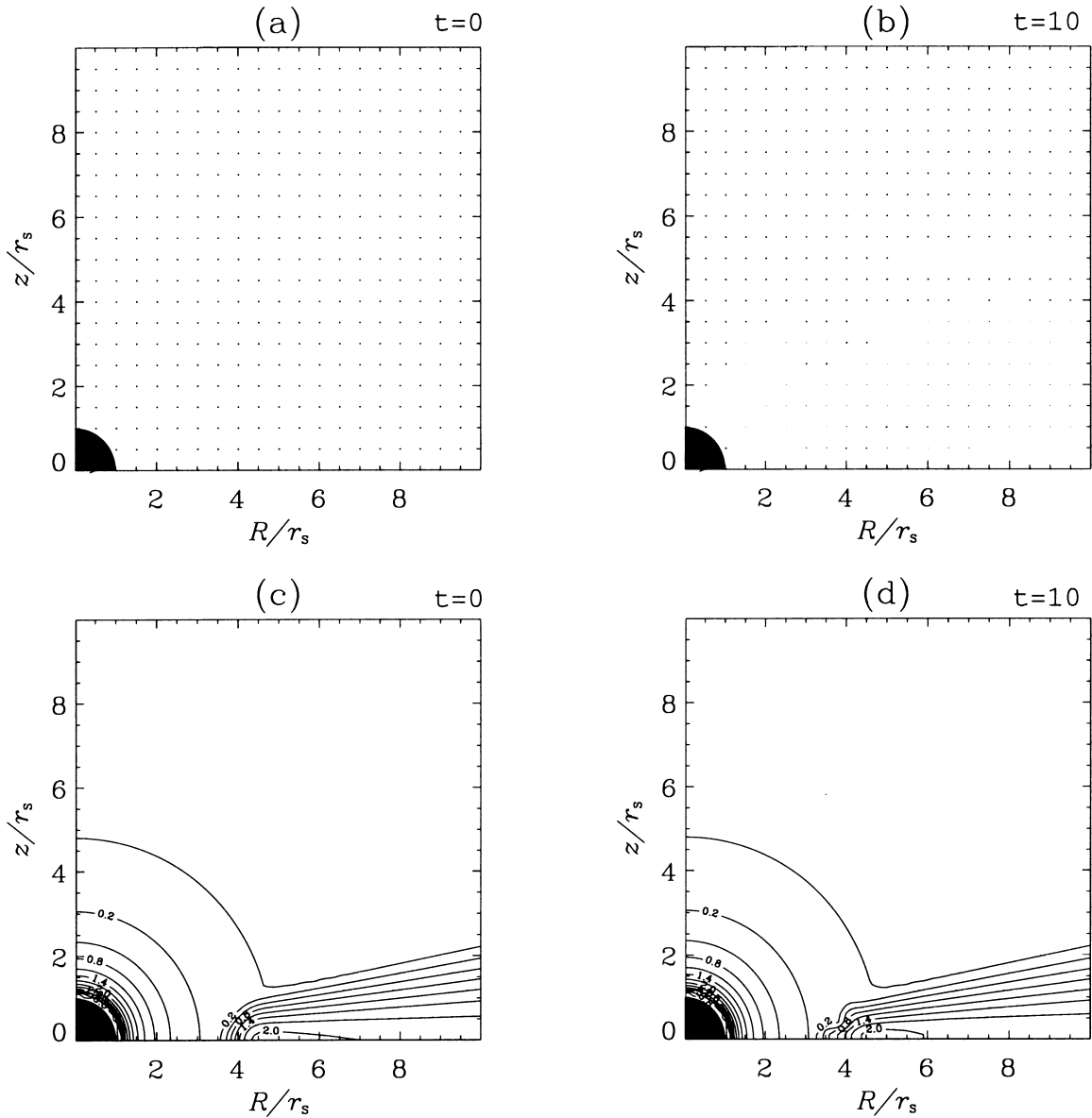


FIG. 5.—Results of Keplerian disk motion in a hydrostatic equilibrium corona. The conditions of the corona are $\Gamma = 5/3$ and $v_s = 0.4c$. The density of the Keplerian disk is 400 times that of the background corona. Black circle shows the black hole. (a) The initial poloidal velocity. (b) The poloidal velocity at $t = 10\tau_s$. (c) The initial proper mass density. (d) The proper mass density at $t = 10\tau_s$. The Keplerian disk is calculated stably.

It is remarkable that the sub-Keplerian disk does not fall into the black hole monotonically; this behavior is important for the formation of the jet around the black hole.

3.5. Keplerian Motion in a Hydrostatic Corona

To check the code, we also computed the Keplerian motion of a disk embedded in a hydrostatic corona around a Schwarzschild black hole (black region in Fig. 5). The disk is located at the same place as in the previous section, but the mass density of the disk is 400 times that of the background corona. Here the hydrostatic corona around the black hole is given by

$$\rho_{\text{hsc}} = \rho_0 \exp \left\{ -\frac{\Gamma}{v_s^2} c^2 [\log h_0 - \log h_0(r_D)] \right\}, \quad (23)$$

$$p = \frac{v_s^2}{1 - v_s^2/(\Gamma - 1)c^2} \frac{\rho_{\text{hsc}}}{\Gamma}, \quad (24)$$

where ρ_0 is the proper coronal mass density at $r = r_D = 3r_s$, v_s is the constant sound velocity of the fiducial observer, $v_s \equiv c(\Gamma p/h)^{1/2}$, $h \equiv \rho c^2 + \Gamma p/(\Gamma - 1)$. We set $v_s = 0.41c$.

Figures 5a and 5c show the initial poloidal velocity and proper mass density, respectively. The calculation region is $r \leq 20r_s$ with the modified tortoise coordinates. The high-density region is located in the disk and near the black hole horizon; the toroidal (azimuthal) velocity component is the relativistic Keplerian velocity, while the poloidal component vanishes initially. At $t = 10\tau_s$, the inner edge of the disk falls slightly toward the black hole, which is seen as a change in the density at the inner edge of the disk (Fig. 5d). However, compared with the initial Keplerian velocity, the infall velocity is too small to be seen in the velocity plot (Fig. 5b), where the unit length of the vector corresponds to the light speed c . This falling motion is due mainly to the smoothing of the initial azimuthal velocity. This result confirms that the stable state of the Keplerian disk and hydrostatic equilibrium are calculated properly by the code.

4. JET FORMATION FROM MAGNETIZED DISK IN A FREE-FALL CORONA

4.1. Initial and Boundary Conditions

The initial state of the simulation consists of two parts: a background corona around the black hole and an embedded accretion disk (Fig. 6a). In this section, the coronal plasma initially consists of a transonic free-fall flow (as in the transonic flow test cases) with $\Gamma = 5/3$ and $H = 1.3$ (§ 3.3). Here the sonic point is located at $r = 1.6r_s$. The accretion disk is located at $|\cot \theta| \leq 0.125$, $r \geq r_D = 3r_s$ and rotates around the black hole with the Keplerian velocity $v_K = c/[2(r/r_s - 1)]^{1/2}$. In this case, the rotational velocity of the disk is 50 % of light velocity at its inner edge ($r = 3r_s$, $z = 0$). The mass density of the disk is 100 times that of the background corona.

In addition, a magnetic field threads the accretion disk vertically. We use the Wald solution for a nonrotating black hole: $B_r = B_0 \cos \theta$, $B_\theta = -\alpha B_0 \sin \theta$, which describes a uniform magnetic field around a Kerr black hole (Wald 1974). At the inner edge of the accretion disk, the proper Alfvén velocity is $v_A = 0.015c$ in a typical case with $B_0 = 0.3(\rho_0 c^2)^{1/2}$, where Alfvén velocity in the fiducial observer is defined by

$$v_A \equiv \frac{B}{\sqrt{\rho + [\Gamma p/(\Gamma - 1) + B^2]/c^2}}. \quad (25)$$

The plasma beta of the corona at $r = 3r_s$ is $\beta \equiv p/B^2 = 1.40$.

The simulation is performed in the region $1.1r_s \leq r \leq 20r_s$, $0 \leq \theta \leq \pi/2$, with 211×71 mesh points, assuming axisymmetry with respect to z -axis and mirror symmetry with respect to the plane $z = 0$. The mesh spacings at $r = 1.1r_s$ and $r = 20r_s$ are $2.6 \times 10^{-3} r_s$ and $0.52r_s$, respectively, and the mesh angular spacing along the polar direction is 2.2×10^{-2} rad. A radiative boundary condition is employed at $r = 1.1r_s$ and $r = 20r_s$:

$$u_0^{n+1} = u_0^n + u_1^{n+1} - u_1^n, \quad (26)$$

where superscripts $n+1$ and n indicate the time step number and the subscripts 0 and 1 show the boundary and its neighbor mesh points, respectively. The computations were performed on SX-4 supercomputers with 300 megabytes internal memory and required 7 hr of CPU time for about 6000 time steps with 211×71 mesh points.

4.2. Jet Formation in a Free-Fall Corona

Figure 6 shows the time development of the jet formed in a free-fall corona with a uniform magnetic field $B_0 = 0.3(\rho_0 c^2)^{1/2}$. Here ρ_0 is the proper mass density of the corona at $r = 3r_s$. These figures show the proper mass density (*color*), velocity (*vector*), and magnetic field (*solid lines*) in $0 \leq R \equiv \sin \theta \leq 10r_s$, $0 \leq z \leq 10r_s$. The black regions indicate the black hole inside the event horizon $r = r_s$. Figure 6b shows a snapshot at $t = 10\tau_s$, after the inner edge of the disk has rotated a quarter cycle of circular orbit, where τ_s is defined as $\tau_s \equiv r_s/c$. The coronal plasma falls rapidly into the black hole, dragging the magnetic field with it and strongly bending the field lines near the black hole. The disk also drags the magnetic field in the azimuthal direction, transferring angular momentum outward in the process and falling toward the black hole. At $t = 40\tau_s$, the inner edge of the disk enters into the unstable orbit region $r \leq 3r_s$ (see Fig. 6c). However, the advection

flow in the unstable orbit region stops at $r \sim 2r_s$, and the plasma in the surface layer of the disk begins to be ejected in the z -direction around the point. The dense disk gas extends along with the ejected gas into the corona perpendicularly to the disk.

In the final stage ($t = 52\tau_s$), a jet is formed from the inner edge of the disk after the edge has rotated more than one cycle (Fig. 6d). The maximum poloidal velocity of the jet is subrelativistic, $\sim (0.2-0.3)c$. The total velocity is $0.38c$ and exceeds the escape velocity in the corona. We find the dense plasma spreads along the jet. It is remarkable that the jet is formed even in the free-fall corona and that the magnetized Keplerian disk continues to exist near the black hole $r \sim (2-3)r_s$. The magnetic field near the black hole becomes radial owing to the fast infall of the plasma.

Next we investigate the mechanism and structure of the jet that forms. Figure 7 shows the physical variables in the final stage at $z = 0$. Initially, the disk was stationary, but by this stage it is falling into the central object rapidly. The disk accretion flow is supersonic: the sound velocity at $r = 4r_s$, for example, is $0.13c$ (so the Mach number $M_D \sim 2$). This supersonic accretion flow then is stopped by a centrifugal barrier (at $r \sim 2r_s$) to form a shock wave at $r = 3r_s$. The strength of the shock is $\rho_d/\rho_u = 1.4$, where ρ_d and ρ_u are the proper mass density at down-stream and up-stream of the shock, respectively. As expected, the flow down-stream of the shock wave is subsonic where the sound velocity is $0.22c$ ($M_D \sim 0.9$). The high pressure is caused by shock and adiabatic heating due to the strong deceleration of the flow, which yields the relativistic region ($p \sim \rho c^2$). As we show later, this high pressure is one of the main sources of jet formation energy. Here we note that the magnetic field pressure B_z^2 is much smaller than the gas pressure p except near the inner edge of the disk (Fig. 7a).

Figure 7b shows the power in the gas pressure and electromagnetic forces that is used to accelerate or decelerate the plasma motion

$$W_{gp} \equiv -\mathbf{v} \cdot \nabla p, \quad (27)$$

$$W_{EM} \equiv \mathbf{v} \cdot (\mathbf{E} + \mathbf{J} \times \mathbf{B}), \quad (28)$$

in the fiducial observer frame (see Appendix B). The plots of $-W_{gp}$ and $-W_{EM}$ show the power contribution for deceleration of the plasma, in particular, the accretion disk itself. It is natural that the deceleration by the gas pressure is significant at the shock front at $R \sim 3r_s$. Below the shock, the deceleration effect decreases drastically and the infall velocity increases again. However, owing to the centrifugal barrier, the plasma stops almost completely at $r = 2r_s$ (Fig. 7d). Both the gas pressure and the electromagnetic forces decelerate the plasma (Fig. 7b), but above the reverse shock the deceleration by the electromagnetic force is somewhat larger than that of the gas pressure ($R > 3r_s$), over the wide region, $R \leq 6r_s$. This electromagnetic force is due to the magnetic tension of the strongly bent magnetic field lines. Based on these facts, the centrifugal force, shock deceleration, and magnetic tension cause a drastic interruption of the disk accretion into the black hole. This interruption is an important step in the formation of the jet. As shown in Figure 7d, the rotation region of the plasma (v_ϕ) extends to $r = 2r_s$. This means that the disk edge accretes to the point $r = 2r_s$ and then stops falling at the point instantly. The

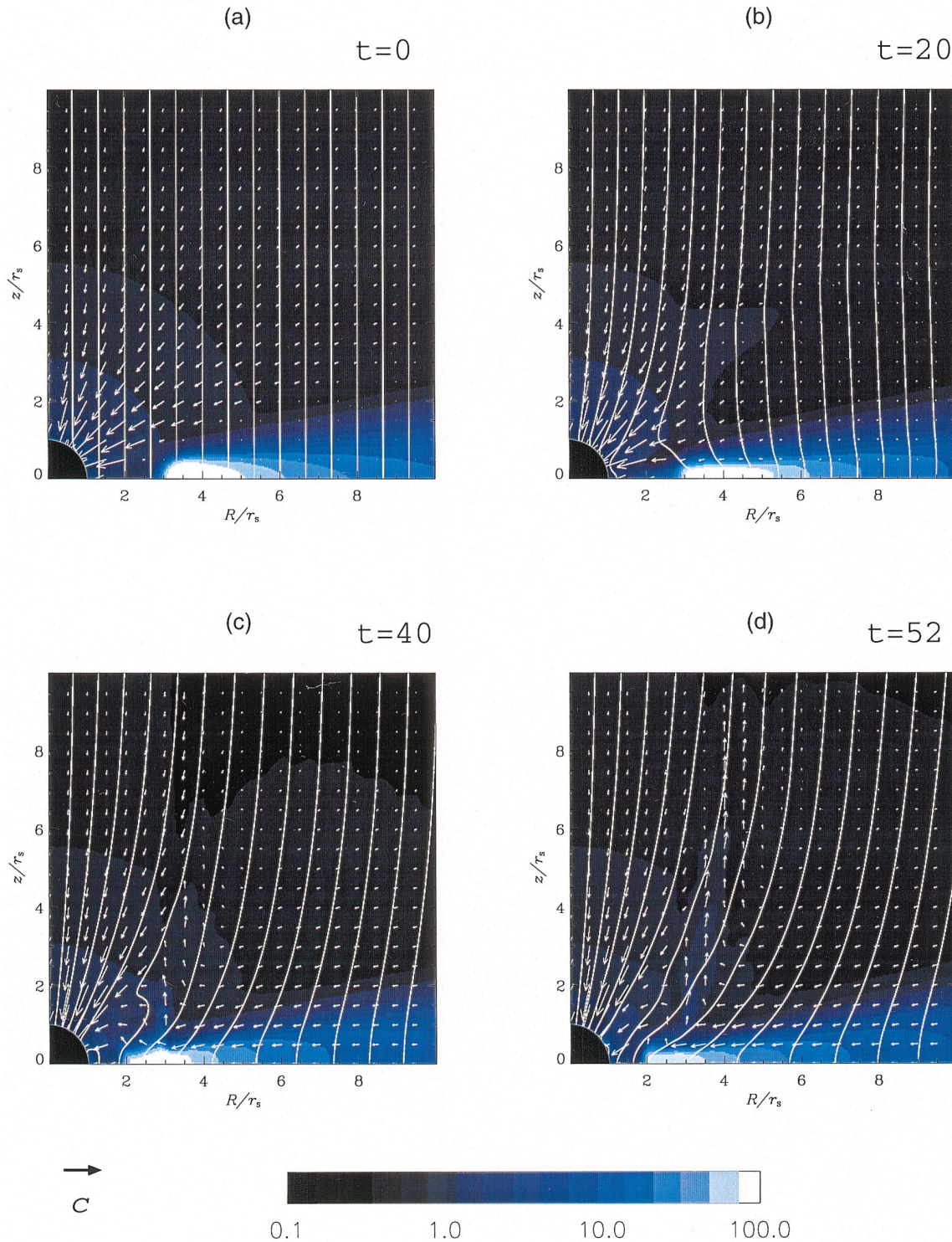


FIG. 6.—Time evolution of the jet formation in a transonic free-fall (steady state falling) corona with an initially uniform magnetic field. The fan-shaped black region indicates a black hole. The solid lines are magnetic field lines. The color shows the proper mass density in a logarithmic scale. The vector plots show the flow velocity. A vector with unit length corresponds to light velocity. Near the horizon, the velocity is almost light speed. (a) The initial condition. The coronal plasma distribution is given by the transonic solution with $\Gamma = 5/3$, $H = 1.3$. The sonic point is located at $r = 1.6r_s$. The disk rotates around the black hole with Keplerian velocity. The density of the disk is 100 times that of the corona. (b) $t = 10\tau_s$. The free-fall corona drags and bends the magnetic field lines near the black hole. (c) $t = 40\tau_s$. The strong deceleration of the accretion of the disk plasma is seen at $r = 3r_s$. (d) $t = 52\tau_s$. The jet is formed almost along the magnetic field. The maximum poloidal velocity of the jet is subrelativistic, $(0.2-0.3)c$. However, the total velocity is $0.38c$ and clearly beyond the escape velocity from the black hole. The distance and the time are in units of r_s and $\tau_s \equiv r_s/c$, respectively.

magnetic field is compressed by the disk edge very strongly (Fig. 7c). This magnetic pressure also contributes to the halting of the disk infall. Below the watershed point at $r \sim 2r_s$, the gas is accelerated rapidly to relativistic velocities

near the horizon, $R \leq 1.7r_s$ (Fig. 7d). The drastic deceleration and the rapid acceleration create an inner edge to the high-density region, which may corresponds to the edge observed by X-rays (Bromley et al. 1998).

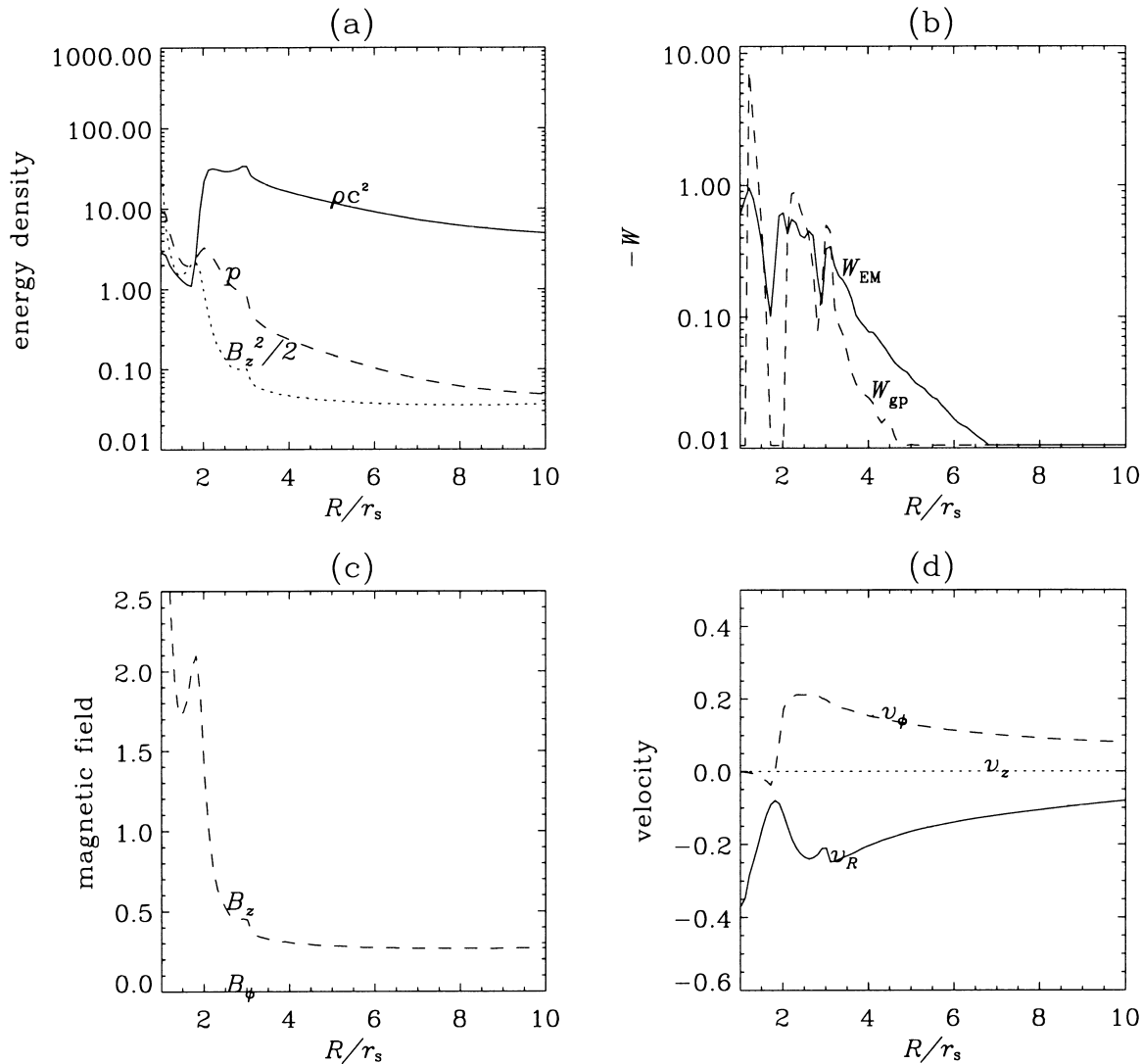


FIG. 7.—Various physical quantities on the equatorial plane, $z = 0$ at $t = 52\tau_s$, in the free-fall (steady state falling) corona case. (a) Proper mass density ρ (solid line), proper pressure p (dashed line), and magnetic field energy $B_z^2/2$ (dotted line). (b) The power contribution of the gas pressure, W_{gp} (dashed line), and the electromagnetic force, W_{EM} (solid line), to evaluate the deceleration effect of the accreting disk plasma. (c) The components of the magnetic field, B_ϕ and B_z . (d) The components of the velocity, v_R , v_z , and v_ϕ . We can see the shock front at $r = 3r_s$.

Figure 8 shows the physical variables along the line $z = 5.6r_s$ at $t = 52\tau_s$. The positive axial component of the velocity $v_z > 0$ shows that the jet spreads in the region: $3.4r_s \leq R \leq 5r_s$ (Fig. 8d). Figure 8a shows that the jet has a two-layered shell structure. The inner part of the jet ($3.4r_s \leq R \leq 4.3r_s$) has high density and pressure compared to the outer part ($4.3r_s \leq R \leq 5r_s$). Figure 8b shows the power contribution of the gas pressure (dashed line) and the electromagnetic force (solid line), W_{gp} and W_{EM} , respectively. We find that the inner part of the jet is accelerated by the gas pressure and the outer part by the electromagnetic force. Therefore, we call the inner part the *gas-pressure-driven jet* and the outer part the *magnetically driven jet*. This two-layer shell structure is also found in the hydrostatic corona case (Koide, Shibata, & Kudoh 1998), as shown in detail in the following § 5. It is natural that the gas-pressure-driven part of the jet has high pressure (Fig. 8a) and that the electromagnetically driven part has the large magnetic field B_ϕ , B_z (Fig. 8c) and the large azimuthal velocity v_ϕ (Fig. 8d). The magnetic field component B_ϕ accelerates the jet through a magnetic pressure gradient, and the azimuthal

velocity v_ϕ accelerates via centrifugal force. These characteristics of the outer jet are the same as those of the nonrelativistic MHD simulation of the magnetically driven jet (Shibata & Uchida 1986). However, the inner jet driven by the gas pressure has never been found in nonrelativistic simulations of the thin-disk model, while in the thick-disk model, similar pressure-driven jets have been reported (Molteni, Lanzafame, & Chakrabarti 1994; Bell & Lucek 1995).

To clarify the acceleration structure of the magnetically driven jet, we plot the physical variables almost along the jet at $R = 4.5r_s$ (Fig. 9). The point $z = 0$ is located at the equatorial plane. As shown in Figure 9a, the density in the disk is high, and the pressure and the magnetic field component are almost constant. Figure 9b shows that the electromagnetic force accelerates the jet at $2.5r_s \leq z \leq 7r_s$ and we can see the increase of the jet velocity v_z (Fig. 9c). This part of the jet corresponds to the outer jet part. A decrease in v_z at $8r_s \leq z$ occurs because the jet does not yet reach the steady state. Figure 9d shows the Alfvén velocity v_A , the sound velocity v_s and the poloidal component of the veloc-

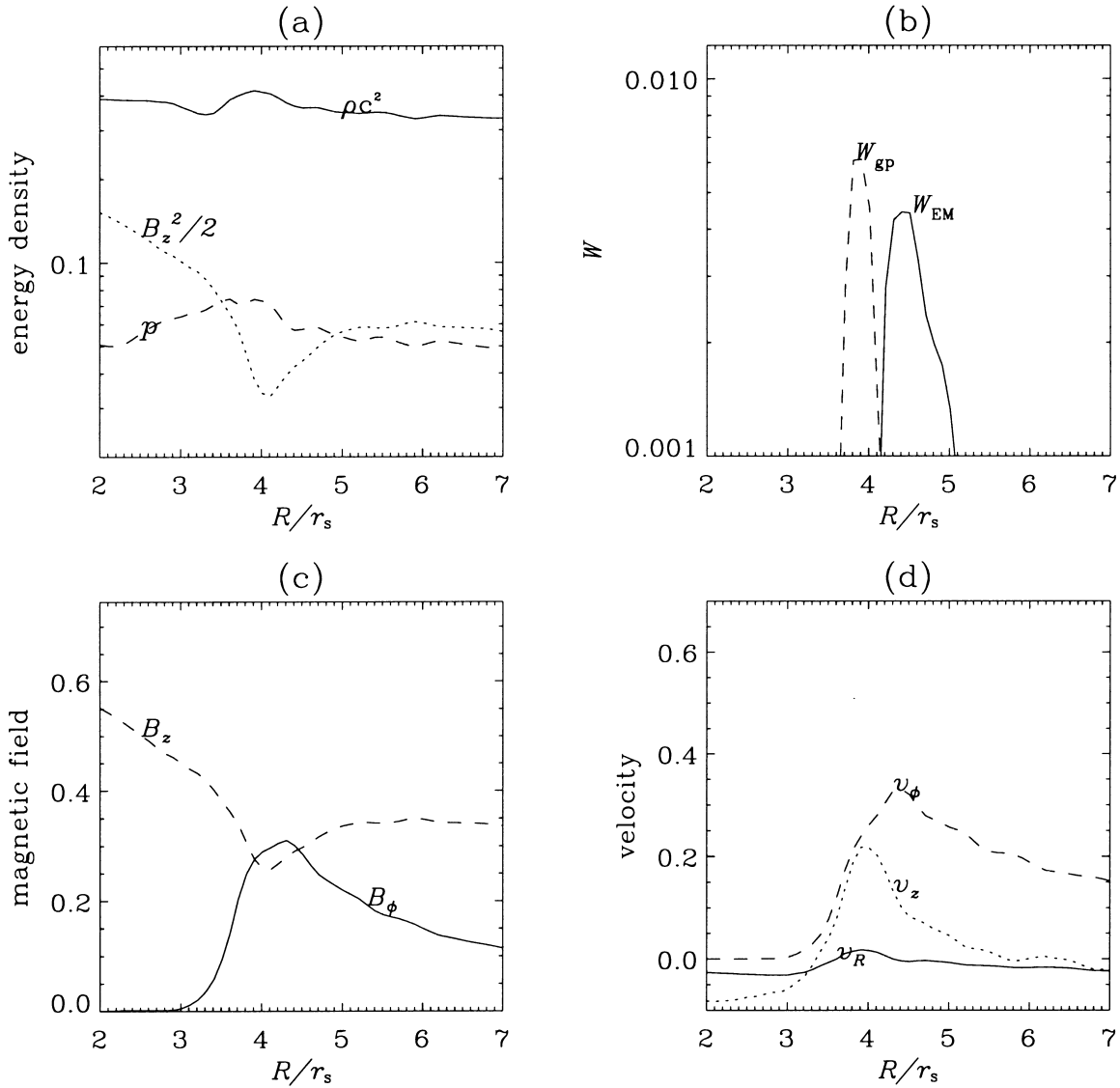


FIG. 8.—Various physical quantities on the $z = 5.6r_s$ surface at $t = 52\tau_s$ in the free-fall (steady state falling) corona case. (a) Proper mass density ρ (solid line), proper pressure p (dashed line), and magnetic field energy $B_z^2/2$ (dotted line). The jet is located around $R = 3.8r_s$. (b) The power contribution of the gas pressure, W_{gp} (dashed line), and the electromagnetic force, W_{EM} (solid line), to evaluate the acceleration of the jet. We can clearly see the two-layer acceleration region in the jet. (c) The components of the magnetic field, B_ϕ and B_z . (d) The components of the velocity, v_R , v_z , and v_ϕ . The jet spreads through $3r_s \leq R \leq 5r_s$.

ity v_p . The poloidal velocity increases in the magnetically driven region $3.5r_s < z < 7r_s$. However, it does not exceed the Alfvén velocity v_A nor the sound velocity v_s . Note that the magnetically driven jet comes from the corona. We can also see the weak gas-pressure-driven region at $7r_s \leq z \leq 9r_s$, which corresponds to the inner part of the jet. In this cross section, the pressure-driven power is too small to show the acceleration clearly, while at the other part ($R \sim 3.8r_s$) pressure-driven power is more dominant than the magnetically driven power, as shown in Figure 8b. The structure of the inner, gas pressure-driven jet is the same as that in the hydrostatic equilibrium coronal case (Koide et al. 1998), and the details are shown in § 5.3.

We also examine the jet ejection rate and the accretion rate of this case at $t = 52\tau_s$. To compute these values, we calculate the inflow and outflow across the cylinder surface $R = 8r_s$, $z = \pm 8r_s$. The accretion rate and the mass-loss rate are $\dot{M}_{ac} = 22\rho_0 r_s^2/\tau_s$ and $\dot{M}_j = 5.8\rho_0 r_s^2/\tau_s$, respectively. Therefore the transformation rate of the disk gas to the jet is

$\dot{M}_j/\dot{M}_{ac} = 0.26$. The accretion rate \dot{M}_{ac} will be compared with the observation in § 6.

4.3. Parameter Dependence

To investigate the jet formation mechanism, we performed parameter surveys of the pressure (H), the mass density of the disk ($\eta_D \equiv \rho_D/\rho_c$, ρ_D and ρ_c are the proper mass density of the disk and the corona, respectively), and the magnetic field (B_0).

Table 1 summarizes the results of the simulations in the transonic free-fall corona cases. Here v^{pres} and v_p^{pres} are the total and poloidal velocities of the pressure-driven jet, respectively, and v^{mag} and v_p^{mag} are those of the magnetically driven jet. The dimensionless parameters $E_{mag} \equiv (v_A/v_K)^2$ and $E_{th} \equiv (v_s/v_K)^2/\Gamma$ are also shown for reader's convenience (e.g., see Kudoh & Shibata 1997a). Case A is the standard case, which already has been shown in the previous subsections. The velocities of all cases are measured at $t = 50\tau_s$. In all cases, the total velocity, v^{pres} is comparable to the

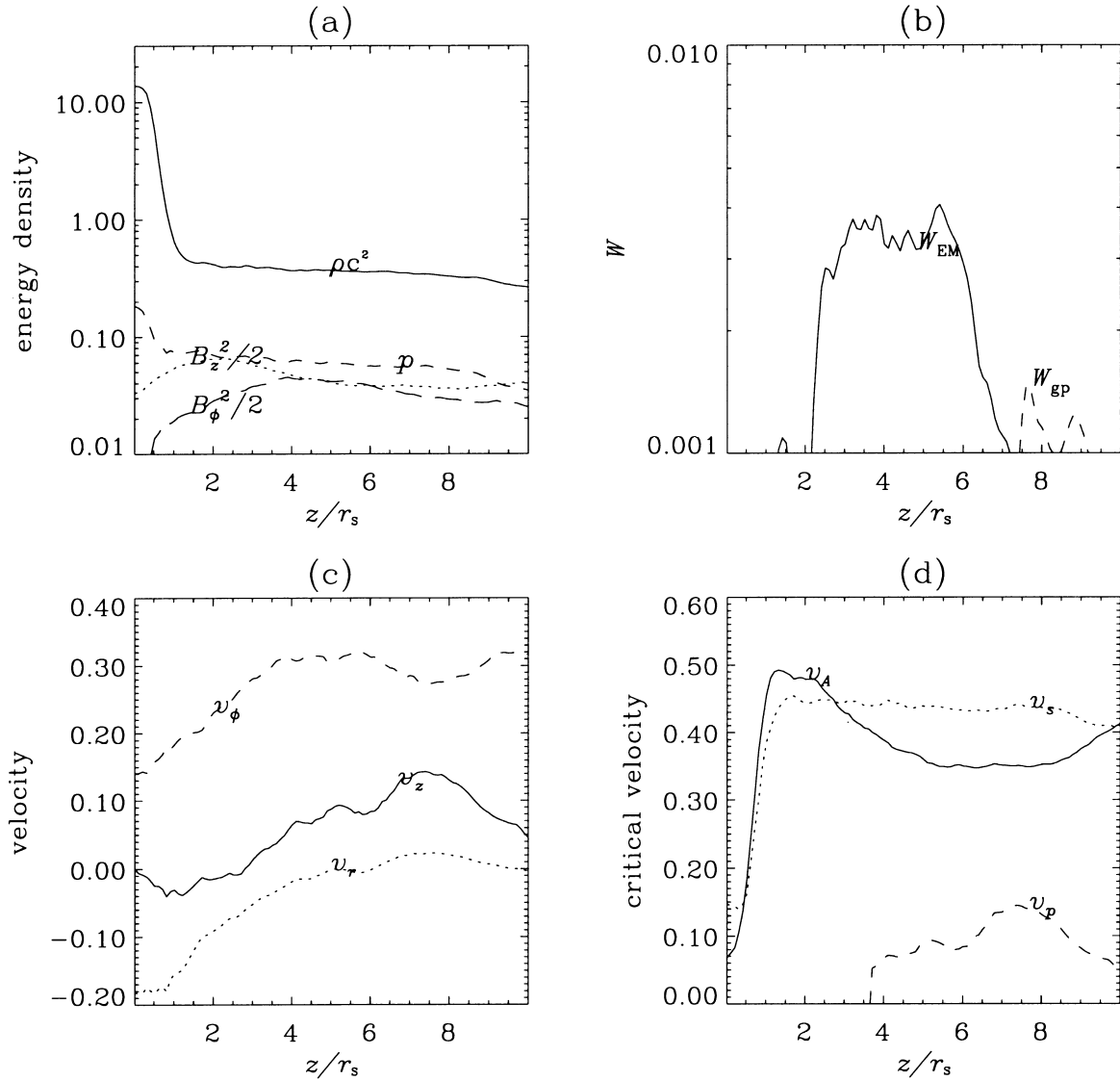


FIG. 9.—Various physical quantities of the free-fall (steady state falling) corona case on the $R = 4.5r_s$ surface at $t = 52\tau_s$. (a) Proper mass density ρ (solid line), proper pressure p (dashed line), and components of the magnetic field energy, $B_\phi^2/2$ (long-dashed line) and $B_z^2/2$ (dotted line). (b) The power contribution of the gas pressure, W_{gp} (dashed line), and the electromagnetic force, W_{EM} (solid line), to evaluate the acceleration of the jet. The magnetically driven region $4r_s \leq z \leq 7r_s$ corresponds to the outer part of the jet. The pressure-driven region $7r_s \leq z \leq 9r_s$ is the inner part. (c) The components of the velocity, v_R , v_z , and v_ϕ . (d) The Alfvén velocity, v_A , the sound velocity, v_s , and the poloidal component of the velocity, v_p . The poloidal velocity, v_p , gradually increases in the magnetically driven region, $7r_s \leq z \leq 9r_s$, but does not exceed both the sound and Alfvén velocities.

poloidal component of the jet velocity, v_p^{pres} for the gas-pressure-driven jet, while the poloidal velocity, v_p^{mag} is smaller than almost half of the total velocity, v^{mag} for the magnetically driven jet. This is a reasonable result, because the pressure can accelerate the gas only in the poloidal direction owing to the assumption of symmetry in the azimuthal direction ϕ . On the other hand, the energy of the magnetically driven jet originates from the azimuthal kinetic energy, and the azimuthal velocity of the magnetically driven jet remains finite in our results. Note that the velocities of the pressure-driven jets, v^{pres} are smaller than the total velocities of the magnetically driven jets, v^{mag} in almost all cases. On the other hand, the poloidal velocities of the pressure-driven jets, v_p^{pres} are larger than those of the magnetically driven jets, v_p^{mag} except the case D.

The dependence on the disk density η_D (cases B, A, and C) shows that the velocity (both total and poloidal velocities) increases as the disk density increases both for the pressure-

driven and the magnetically driven jets. This comes from the fact that the total kinetic energy of the heavier disk is larger than that of the lighter disk. Note that the maximum velocity of the jet in all cases is subrelativistic, $(0.3\text{--}0.4)c$.

The dependence on the initial magnetic field strength B_0 (cases D, A, E, and F) shows that the pressure-driven jets are accelerated faster as B_0 increases. On the other hand, the velocity (both total and poloidal velocities) of the magnetically driven jet decreases as B_0 increases. The faster pressure-driven jet is explained as follows: a stronger magnetic field decelerates the accretion disk more rapidly and forms a higher pressure region near the centrifugal watershed; this higher pressure produces faster acceleration. The slower, magnetically driven jet is opposite to that expected by the steady state theory. The reason is not clear, but may be related to time-dependent effects. For a long enough simulation, a steady state should occur and the theoretically predicted dependence on B_0 should be found. With the

TABLE 1
PARAMETER DEPENDENCE IN THE FREE-FALL (STEADY STATE FALLING) CORONA CASES

Case ^a (1)	Different Parameter (2)	v_p^{pres} (c) (3)	v^{pres} (c) (4)	v_p^{mag} (c) (5)	v^{mag} (c) (6)	E_{mag} (7)	E_{th} (8)
A	Standard	0.22	0.22	0.15	0.30	0.75×10^{-2}	1.2×10^{-2}
B	$\eta_D = 50$	0.13	0.15	0.09	0.30	1.5×10^{-2}	2.4×10^{-2}
C	$\eta_D = 200$	0.24	0.26	0.20	0.32	0.37×10^{-2}	0.62×10^{-2}
D	$B_0 = 0.25$	0.12	0.17	0.17	0.30	0.51×10^{-2}	1.3×10^{-2}
E	$B_0 = 0.4$	0.23	0.24	0.13	0.30	1.3×10^{-2}	1.2×10^{-2}
F	$B_0 = 0.5$	0.22	0.24	0.10	0.27	2.1×10^{-2}	1.2×10^{-2}
G	$H = 1.05$	0.34	0.35	0.18	0.37	0.75×10^{-2}	0.31×10^{-2}
H	$H = 1.1$	0.28	0.36	0.14	0.34	0.75×10^{-2}	0.48×10^{-2}
I	$H = 1.35$	0.21	0.24	0.11	0.32	0.75×10^{-2}	1.4×10^{-2}

NOTE.—Case A is considered the control ($\eta_D \equiv \rho_D/\rho_c = 100$, $B_0 = 0.3$, and $H = \alpha\gamma\{1 + \Gamma p/[(\Gamma - 1)\rho c^2]\} = 1.3$), and the other cases differ from case A in only one parameter, which is noted in column (2). Col. (3): Poloidal component of the velocity of the pressure-driven jet at $t = 50\tau_s$. Col. (4): Velocity of the pressure-driven jet at $t = 50\tau_s$. Col. (5): Poloidal velocity of the magnetically driven jet at $t = 50\tau_s$. Col. (6): Velocity of the magnetically driven jet at $t = 50\tau_s$. Col. (7): $E_{\text{mag}} \equiv (v_A/v_K)^2$ at $r = 3r_s$, $z = 0$ in the initial disk. Col. (8): $E_{\text{th}} \equiv (v_s/v_K)^2/\Gamma$ at $r = 3r_s$, $z = 0$ in the initial disk.

^a Cases: A, standard case; B, light-disk; C, heavy-disk; D, weak magnetic field; E, moderately strong magnetic field; F, strong magnetic field; G, very low pressure; H, low-pressure; I, high-pressure.

present code, it is difficult to perform a long-term calculation (several hundred τ_s). Very strong magnetic field cases are also problematic because of difficulties near the inner boundary.

The different cases of coronal pressure (i.e., specific enthalpy H ; cases G, H, A, and I) indicate that, for both the pressure-driven and magnetically driven jets, a faster jet is ejected when H is lower. In our simulations, the pressure of the disk is balanced with the corona. Therefore in the low-pressure corona case, resistance to the plasma motion is smaller while the high pressure at the centrifugal barrier remains the same, resulting in a faster jet.

5. JET FORMATION IN A MAGNETIZED DISK WITH A HYDROSTATIC CORONA

To compare relativistic and nonrelativistic calculations (Shibata & Uchida 1986) directly, we also computed the hydrostatic corona case (Koide et al. 1998). This could occur in situations with strong radiation near the horizon, resulting in a balance between radiation pressure and strong gravity (Rees 1984).

5.1. Initial and Boundary Conditions

In this section, the coronal plasma is assumed to be in hydrostatic equilibrium (Fig. 10a), where the proper sound velocity is constant ($v_s = 0.41$). The accretion disk is located at $|\cot \theta| \leq 0.125$, $r \geq r_D = 3r_s$ and rotates around the black hole with the Keplerian velocity $v_K = c/[2(r/r_s - 1)]^{1/2}$ (as in § 3.5). In this case, the rotational velocity of the disk is also 50% of light velocity at its inner edge ($r = 3r_s$, $z = 0$), and the mass density of the disk is 400 times that of the background corona. As before, the magnetic field threads the accretion disk vertically, and we use the Wald solution (Wald 1974), as we did in the previous cases. At the inner edge of the accretion disk, the proper Alfvén velocity is $v_A = 0.015c$. The simulations are also performed in the region $1.1r_s \leq r \leq 20r_s$, $0 \leq \theta \leq \pi/2$ with 210×70 mesh points.

5.2. Time Development in Relativistic and Nonrelativistic Cases

Figure 10 shows the time development of the relativistic jet in the black hole magnetosphere. These figures show the proper mass density (*gray scale*), velocity (*vector*), and magnetic field (*solid lines*) in $0 \leq R \leq 7r_s$, $0 \leq z \leq 7r_s$. The black regions show the black hole inside the event horizon at the Schwarzschild radius r_s . Note that $v_{A,\text{corona}}(r = 3r_s) = 0.3c$ and the plasma beta, $\beta(r = 3r_s) \equiv p_{\text{gas}}/p_{\text{mag}} \sim 3.7$ in both the corona and the disk.

Figure 10b shows a snapshot at $t = 10\tau_s$, after the disk has rotated a quarter cycle. The Alfvén wave propagates along the magnetic field lines from the disk and the front of the wave reaches $z \sim 5.5r_s$ at this stage. The accretion disk then loses its angular momentum as a result of magnetic braking and begins to fall toward the black hole, as shown in the vector plot of Figure 10b.

A jet begins to be ejected at the inner edge of the accretion disk around $R \sim 2r_s$, $z \sim 0$ at $t = 40\tau_s$ after the disk has rotated one full cycle (Fig. 10c). The plasma in the unstable region begins to fall into the black hole rapidly and collides with the centrifugal barrier and/or the high-pressure corona near the black hole. The plasma then is compressed by this strong collision. Figure 10d shows the final stage of this simulation at $t = 91\tau_s$, after the accretion disk has rotated more than two cycles. The jet grows significantly and propagates almost along the global poloidal magnetic field lines. The jet is ejected from $R \sim 2r_s$, $z \sim 0$. The maximum poloidal component of the jet velocity reaches to $0.88c$ (Lorentz factor 2.1) at $R \sim 3.0r_s$, $z \sim 3.5r_s$. It is remarkable that magnetic field lines are strongly stretched and deformed by the jet. Figure 10d also shows that the jet has a two-layered shell structure, consisting of the inner fast and outer slow jets. Note also that there is flow near the z -axis, which is not seen in the free-fall coronal cases (compare Figs. 6d and 10d). This flow comes from the hydrostatic corona, and is driven by compression of the plasma near the black hole ($R \sim 0$, $z \sim 2r_s$). Similar flows near z -axis are found in all nonrelativistic simulations with

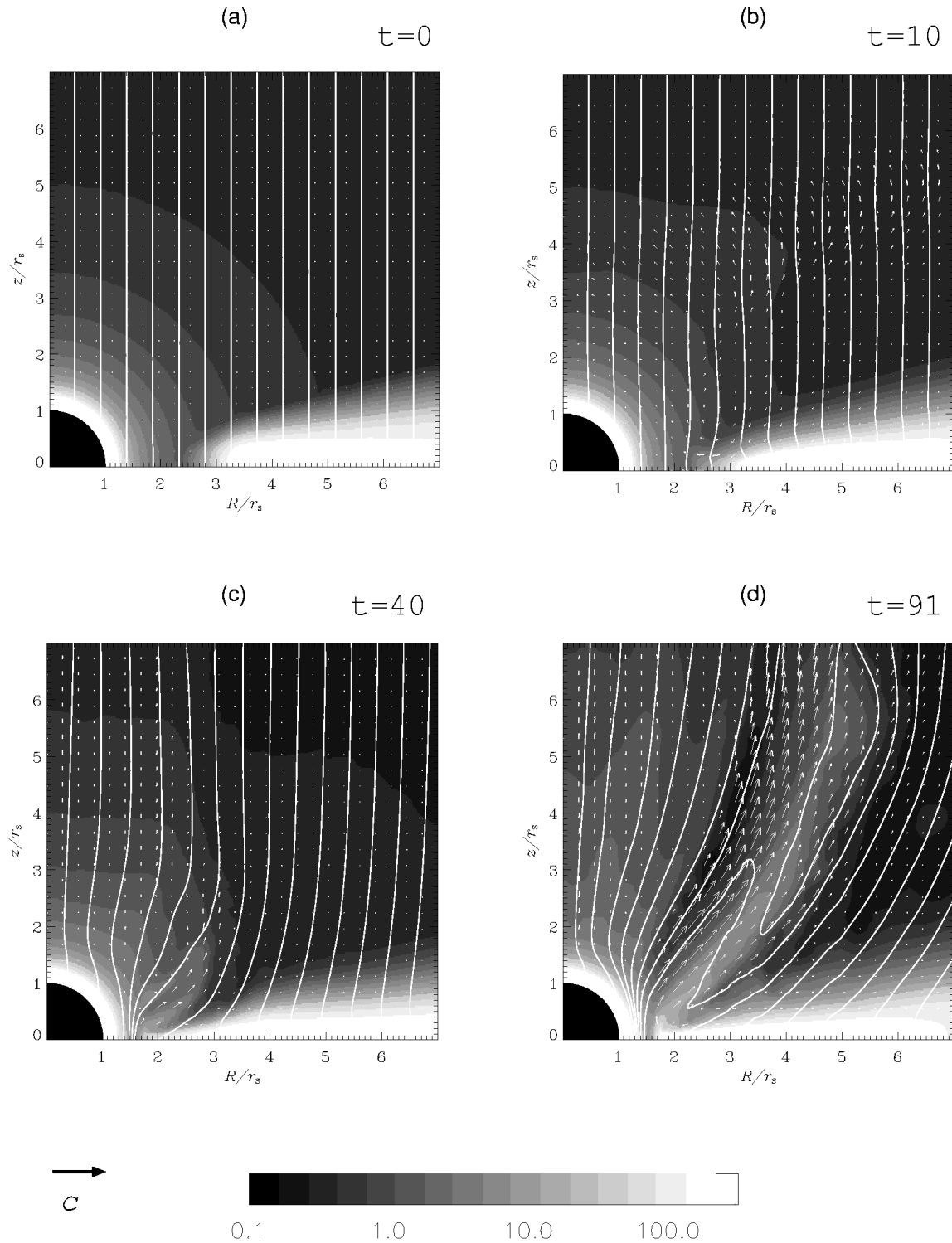


FIG. 10.—Evolution of the jet formation in a hydrostatic black hole magnetosphere. Black region indicates the black hole. The solid lines are magnetic field lines. The gray-scale plots show the proper mass density in a logarithmic scale. The vector plots show the velocity. A vector with unit length corresponds light velocity. (a) The initial condition. The coronal plasma is in hydrostatic equilibrium. (b) $t = 10\tau_s$. The rotating disk drags the magnetic field lines, and the large-amplitude, nonlinear Alfvén wave propagates along the magnetic field from the disk. (c) $t = 40\tau_s$. The jet begins to be ejected from the inner edge of the disk. (d) $t = 91\tau_s$. The relativistic jet is formed almost along the magnetic field lines.

hydrostatic equilibrium coronal conditions (see Fig. 11; Uchida & Shibata 1985; Shibata & Uchida 1986). However, this flow may be unrealistic owing to the unlikely scenario of a hydrostatic corona near a black hole.

Figure 11 shows the result of a nonrelativistic simulation ($v_s = 0.005c$) at $t = 100\tau_0$ for comparison with the rela-

tivistic simulation ($v_s = 0.5c$) (Fig. 10d). Here τ_0 is defined by $\tau_0 \equiv r_0/v_0$ with a characteristic length $r_0 = r_D/3$ and velocity $v_0 = 10^{-2}c = 0.4V_K$, where V_K is the Keplerian velocity at the inner edge of the initial disk, $r = r_D$. The parameters in the nonrelativistic case are almost the same as those in the relativistic one except for the light velocity.

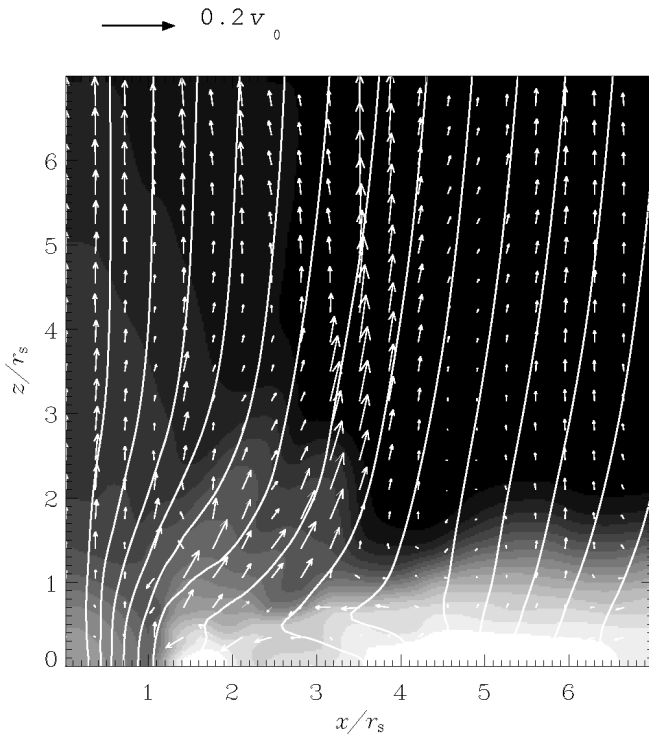


FIG. 11.—Nonrelativistic jet formation at $t = 100\tau_0$, where $\tau_0 \equiv r_0/v_0$, $v_0 = 10^{-2}c$, and $r_0 = r_D/3$. The gray-scale plot shows the proper mass density in a logarithmic scale. The vector is the velocity; the scale normalized by the light velocity is 100 times smaller than that of the relativistic case (Fig. 10). The solid lines show the magnetic field. Only the magnetically driven jet is formed. The maximum poloidal component of the velocity is $\sim 0.4V_K$, where V_K is the Keplerian velocity at the inner edge of the initial disk.

We normalize physical quantities by the proper sound velocity of the corona v_s , the inner radius of the disk r_D , and the proper mass density of the corona at $r = r_D$. The scale of the vectors in the figure of the nonrelativistic case (Fig. 11), when normalized by the light velocity, is 0.01 times that of the relativistic case (Fig. 10). In the nonrelativistic case, the material of the jet originates from the surface layer of the disk, and the maximum poloidal component of the jet velocity is $\sim 0.4V_K$, which is smaller than that in the relativistic cases. The accretion velocity is $\leq 0.1V_K$, which is much slower than that in the relativistic case ($0.25c \sim 0.5V_K$). In the nonrelativistic case, we find that only magnetic forces accelerate the jet gradually, as in the model by Shibata & Uchida (1986).

On the other hand, the relativistic jet in the hydrostatic coronal case has a two-layered shell structure: slow (outer layer) and fast (inner layer) jets as in the free-fall coronal cases. The two jets are separated by the dense flow from $R = 2r_s$, $z = 0$ (Fig. 10d). This dense flow is a part of the pressure-driven jet. In the outer layer, the plasma is accelerated by the magnetic force as in the Shibata & Uchida (1986) model. The low-density part of the jet in the inner layer is accelerated by the gas pressure, and it rapidly reaches the relativistic speed ($0.88c$) within a short distance (several r_s). This rapid acceleration is due to gas highly compressed by the strong gravity of the black hole below the Schwarzschild stable-orbit limit of radius $3r_s$.

5.3. Mechanism and Structure of Relativistic Jet

To confirm the acceleration mechanism of the inner and outer jet, we show the distributions of several physical

quantities across the jet at $z = 2.4r_s$, $t = 91\tau_s$ (Fig. 12). The jet region is identified by the positive poloidal velocity $v_R > 0$, $v_z > 0$. As shown in Figure 12d, the jet is located at $2r_s \leq R \leq 5r_s$. It is clear that there are two peaks of the inner and outer jet velocity. In the outer part, the power from the electromagnetic force dominates the jet acceleration (Fig. 12b). The azimuthal component of the magnetic field (B_ϕ) is larger than the vertical component (B_z) (Fig. 12c), and the magnetic pressure dominates the gas pressure (Fig. 12a). These characteristics are the same as in magnetically driven jets in Newtonian MHD simulation model such as that of Shibata & Uchida (1986), identifying it as a magnetically driven jet. In the inner jet, the mass density and pressure are high compared to the outer part (Fig. 12a), with the high density material coming from the disk (Fig. 10). The power of gas pressure is dominant in the inner jet (Fig. 12b), identifying this flow as pressure-driven. This jet is not found in the corresponding Newtonian MHD simulation with the thin disk (Fig. 11).

As described previously, the inner jet rapidly reaches a relativistic speed within a small distance. (The maximum poloidal component of the jet velocity is $0.88c$ and the acceleration distance is only several r_s .) This rapid acceleration is a result of the rapid pressure increase due to a shock that is formed inside the rapidly infalling disk (i.e., “advection dominated disk”), drawn inward by the strong gravity of the black hole below the last stable Keplerian orbit at $r = 3r_s$. Figure 13 shows physical quantities along the equatorial plane of the disk ($z = 0$) for both the relativistic (panels a and c) and nonrelativistic cases (panels b and d). In the relativistic case, the accretion disk (high-density region) falls into the black hole rapidly and its edge reaches near $r \sim 1.7r_s$ (Fig. 13a). The accretion velocity, v_R , is as large as half of the azimuthal velocity, v_ϕ , because the disk plasma is in the unstable region of the Keplerian motion (Fig. 13c). A shock (a kind of a reverse shock or a Mach disk) is formed inside the rapidly falling disk, greatly increasing the gas pressure and accelerating the disk plasma in both polar directions along global poloidal magnetic fields. Similar shock and jet formation structure are found by Hawley & Smarr (1985) using general relativistic hydrodynamic simulations. On the other hand, in the nonrelativistic case, the accretion velocity is much smaller than the azimuthal velocity (Fig. 13d). In this case, the strength of the shock in the disk is much smaller than that of relativistic case so that the gas pressure increase at the shock is weak (Fig. 13b). Consequently, only a magnetically driven jet is formed in this case.

To confirm the acceleration structure of the relativistic jet, we plot the physical variables almost along the jet at $R = 4.8r_s$ (Fig. 14). The point at $z = 0$ corresponds to the equatorial plane. As shown in Figure 14a, the density of the disk is high and that of the jet is also higher than the other ambient gas. The higher pressure part is seen at $5r_s < z < 8r_s$. In this region, the magnetic pressure is low. This part corresponds to the gas-pressure-driven jet. The high magnetic pressure (low gas pressure) part is located at $3r_s < z < 4.5r_s$, and corresponds to the magnetically driven jet. The difference in the acceleration mechanism of the two regions is shown clearly by the power from the electromagnetic force (W_{EM}) and the gas pressure (W_{gp}) (Fig. 14b). In the gas pressure region ($5r_s < z < 8r_s$), the radial and axial components of the velocity are large, while the azimuthal component is small (Fig. 14c). In the magnetically driven jet ($3r_s < z < 4.5r_s$), the poloidal velocity exceeds the Alfvén

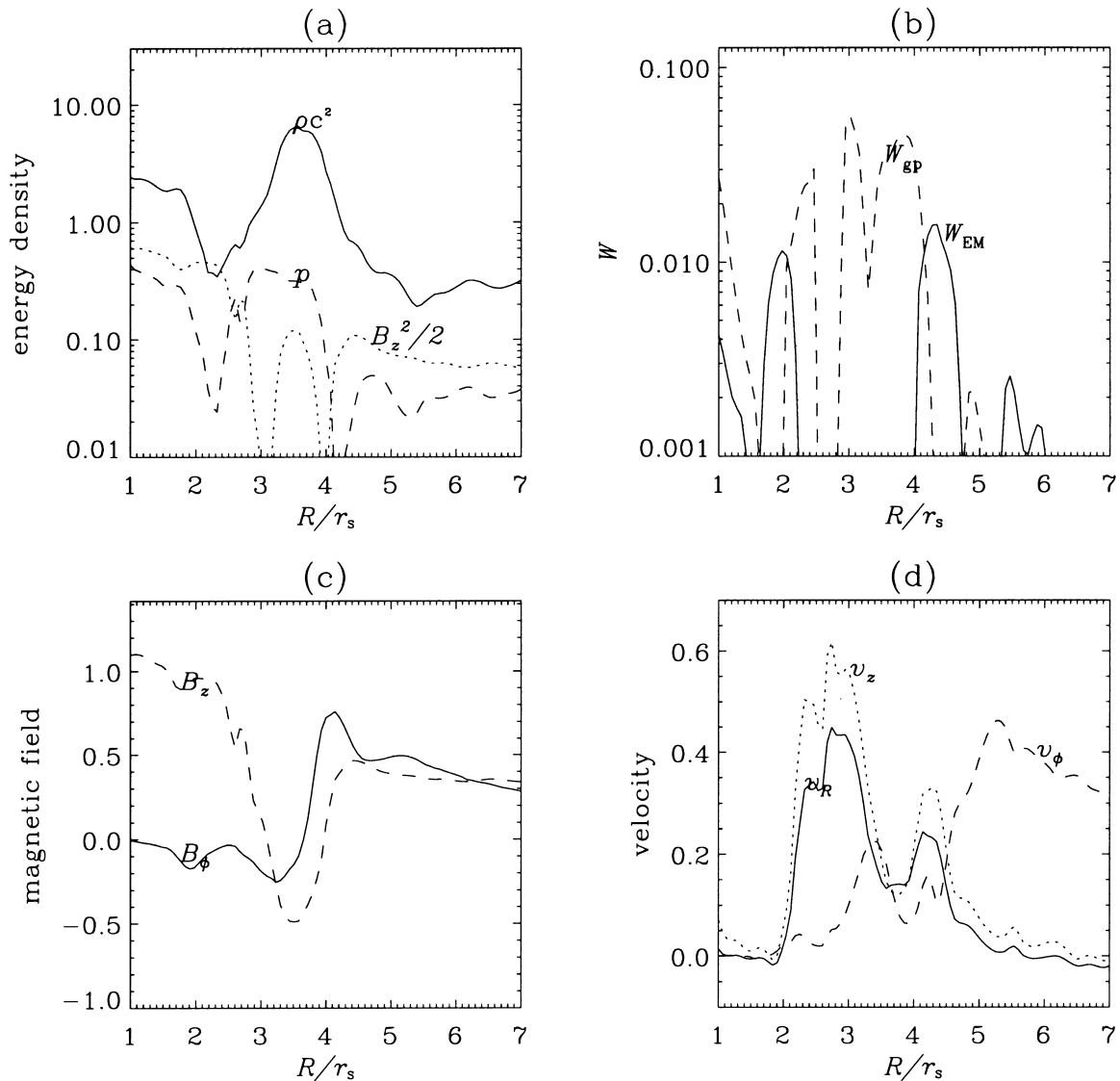


FIG. 12.—Various physical quantities on the $z = 2.4r_s$ surface at $t = 91\tau_s$. (a) The proper mass density ρ , pressure p , and magnetic pressure, $B_z^2/2$. (b) The power density W by the gas pressure W_{gp} (dashed lines) and the electromagnetic force W_{EM} (solid lines) to the jet. (c) Vertical and azimuthal components of the magnetic field, B_z and B_ϕ . (d) Components of the velocity, v_R , v_z , and v_ϕ .

velocity at $z > 3.7r_s$. In the gas pressure jet ($5r_s < z < 8r_s$), the poloidal velocity also exceeds both the Alfvén and sound velocities.

In spite of the vast difference in the initial corona conditions, a similar jet—with a two-layered shell structure—is formed in both the free-fall and hydrostatic cases. A schematic picture of the jet formation is shown in Figure 15. Below the last stable Keplerian orbit $r = 3r_s$, the accretion disk falls into the hole rapidly. A reverse shock is formed in the rapidly falling disk, and a fast jet is formed by the extremely high pressure behind the shock front (gas-pressure-driven jet). A magnetically driven jet is formed in the outer layer of the gas-pressure-driven jet. The main difference between the free-fall and the hydrostatic coronal cases is the existence of direct accretion into the black hole in the former case (heart-shaped region in Fig. 15a) but not in the latter (Fig. 15b). This causes a difference in shock strength, with the shock in the hydrostatic corona case being stronger than that in the free-fall corona case and the pressure-driven jet being faster as well.

The difference in the accretion of disk material into the black hole also causes a difference in magnetic field configuration near the horizon. In the free-fall corona case magnetic field lines near the horizon become radial, whereas they remain almost uniform near the black hole in the hydrostatic corona case.

5.4. Parameter Dependence

To investigate the dependence of the jet velocity on the disk density ($\eta_D \equiv \rho_D/\rho_c$) and the initial magnetic field (B_0), we performed simulations of five cases (see Table 2). Table 2 shows the maximum velocities of each case and area at $t = 70\tau_s$. Case J is the reference case for the parameter survey. Case L is reported in the previous sections. The dependence on the density of the disk (cases K, J, and L) shows that the velocity (both total and poloidal velocities) increases as the density increases for the pressure-driven jet. This is the same tendency as in the free-fall coronal cases. On the other hand, for the magnetically driven jet, the poloidal component of the velocity, v_p^{mag} increases as the disk

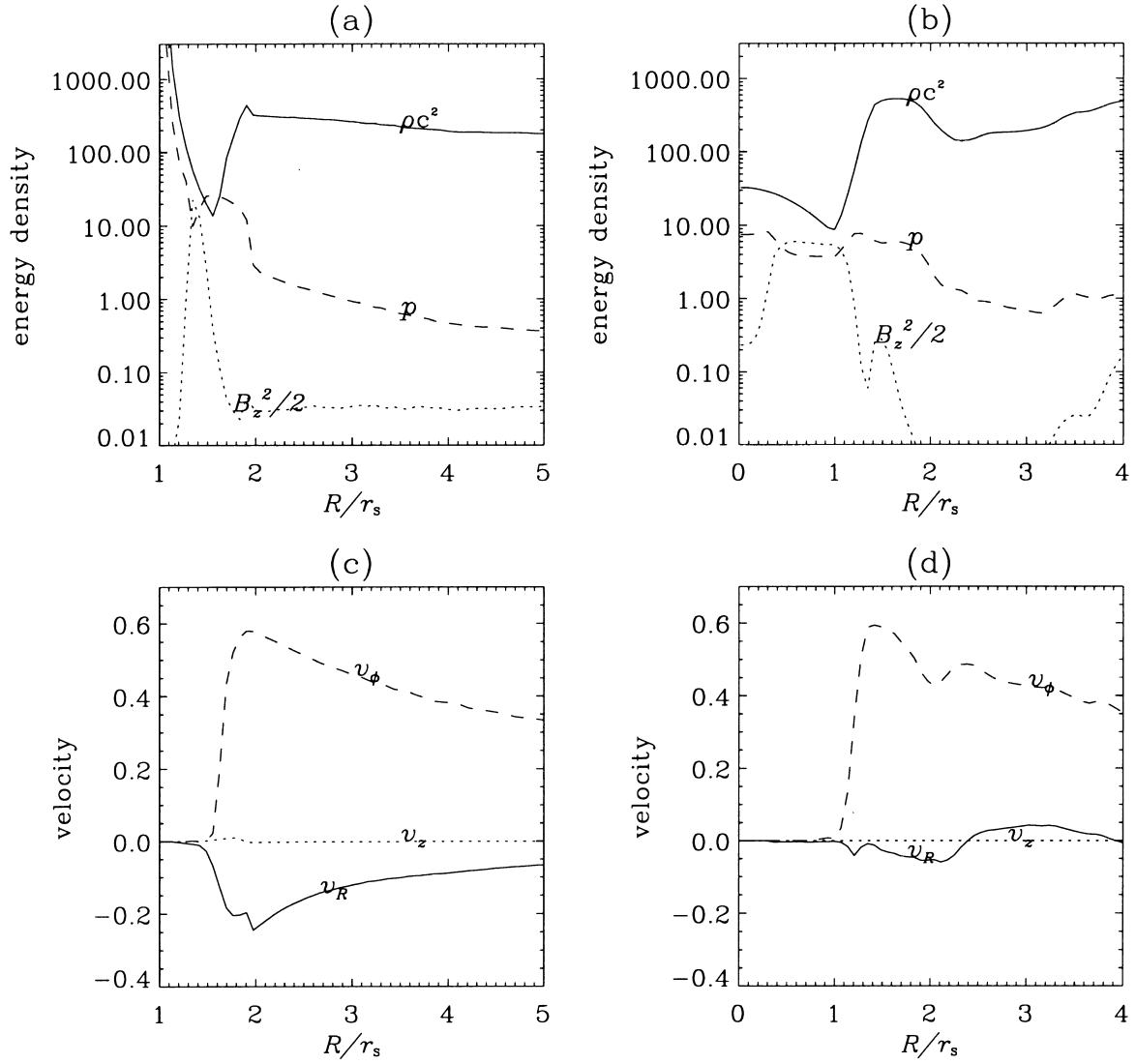


FIG. 13.—Physical variables at the equator for the relativistic case (a, c) and the nonrelativistic case (b, d) at $t = 91\tau_s$ and $t = 100\tau_0$, respectively. Panels a and b show the proper mass density ρ , proper pressure p , and magnetic pressure $B_z^2/2$; panels c and d show the accretion velocity v_R , azimuthal velocity v_ϕ , and axial velocity v_z . In the relativistic case, the accretion disk falls into the black hole rapidly as a result of the strong gravitational force. The reverse shock wave is induced in the accretion disk at $r \sim 2r_s$. In the down stream, the extreme high-pressure region is formed and causes the relativistic jet, with collimation by the magnetic field. In the nonrelativistic case, we do not find such strong shock structure, and only a magnetically driven jet is formed.

TABLE 2
PARAMETER DEPENDENCE IN THE HYDROSTATIC EQUILIBRIUM CORONA CASES

Case ^a (1)	Different Parameter (2)	v_p^{pres} (c) (3)	v_p^{pres} (c) (4)	v_p^{mag} (c) (5)	v_p^{mag} (c) (6)	E_{mag} (7)	E_{th} (8)
J	Standard	0.56	0.56	0.19	0.43	0.30×10^{-2}	0.51×10^{-2}
K	$\eta_D = 100$	0.53	0.54	0.16	0.44	0.56×10^{-2}	1.0×10^{-2}
L	$\eta_D = 400$	0.60 ^b	0.60 ^b	0.21	0.39	0.15×10^{-2}	0.26×10^{-2}
M	$B_0 = 0.25$	0.51	0.51	0.18	0.35	0.13×10^{-2}	0.51×10^{-2}
N	$B_0 = 0.5$	0.54	0.54	0.31	0.43	0.73×10^{-2}	0.48×10^{-2}
	Nonrelativistic	$0.35V_K$	$1.5V_K$	0.23×10^{-2}	0.38×10^{-2}

NOTE.—Case J is considered the control ($\eta_D \equiv \rho_D/\rho_c = 200$, $B_0 = 0.3$, and $v_s = 0.41c$), and the other cases differ from case J in only one parameter, which is noted in column (2). Col. (3): Poloidal component of the velocity of the pressure-driven jet at $t = 70\tau_s$. Col. (4): Velocity of the pressure-driven jet at $t = 70\tau_s$. Col. (5): Poloidal component of the velocity of the magnetically driven jet at $t = 70\tau_s$. Col. (6): Velocity of the magnetically driven jet at $t = 70\tau_s$. Col. (7): $E_{\text{mag}} \equiv (v_s/v_K)^2$ at $r = 3r_s$, $z = 0$ in the initial disk. Col. (8): $E_{\text{th}} \equiv (v_s/v_K)^2/\Gamma$ at $r = 3r_s$, $z = 0$ in the initial disk.

^a Cases: J, standard case; K, light-disk; L, heavy-disk; M, weak magnetic field; N, strong magnetic field.

^b At the final stage in this case ($t = 95\tau_s$), the jet velocity reaches $v_j = 0.88c$, which was reported by Koide et al. 1998.

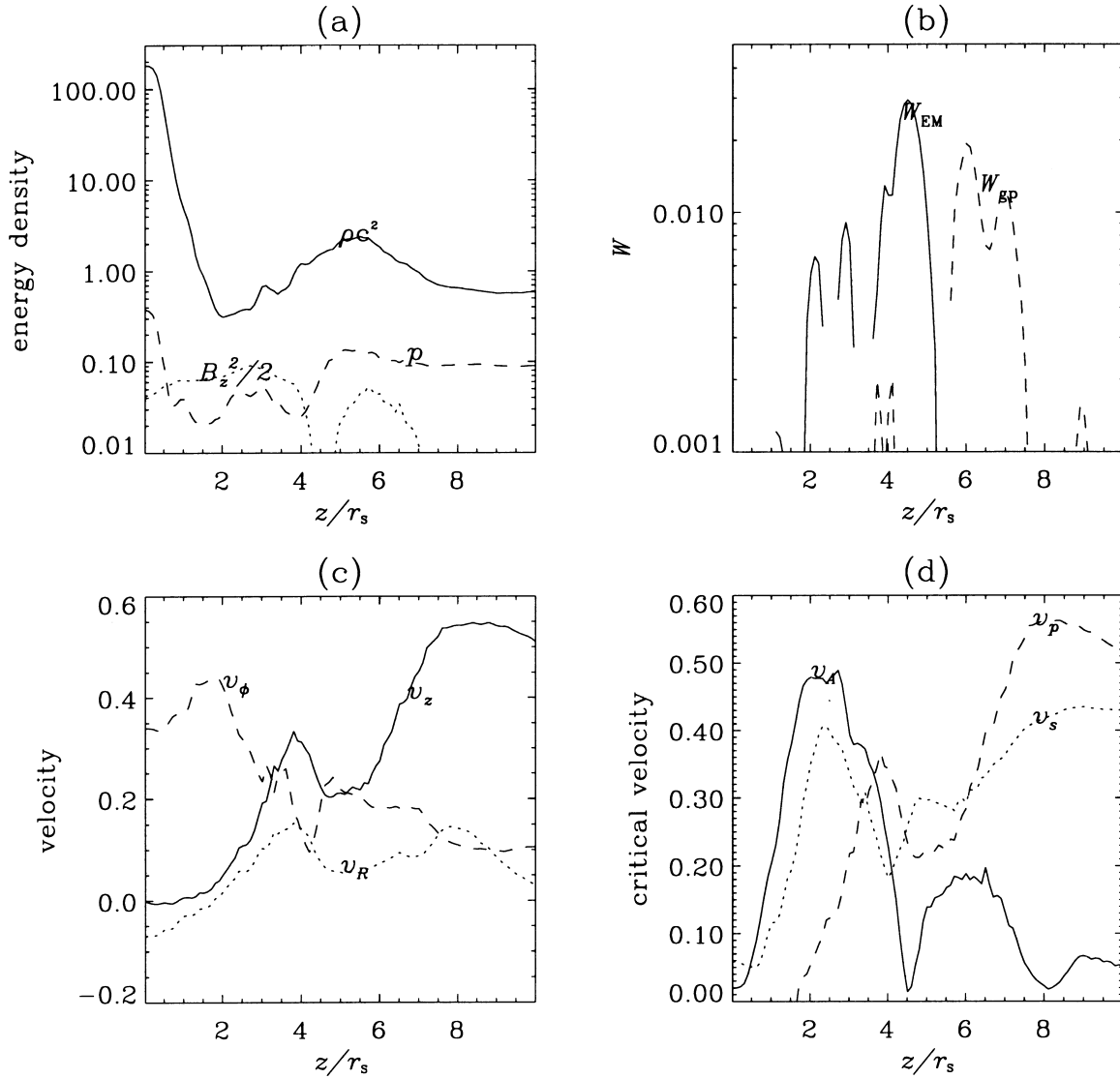


FIG. 14.—Various physical quantities of the equilibrium corona case on the $R = 4.8r_s$ surface at $t = 91\tau_s$. (a) Proper mass density ρ (solid line), proper pressure p (dashed line), and magnetic field energy, $B_z^2/2$ (dotted line). (b) The power contribution of the gas pressure, W_{gp} (dashed line), and the electromagnetic force, W_{EM} (solid line), to evaluate the acceleration of the jet. The magnetically driven region $2r_s < z < 4.5r_s$ corresponds to the outer part of the jet. The pressure-driven region is seen at $5r_s < z < 8r_s$. (c) The components of the velocity, v_R , v_z , and v_ϕ . (d) The Alfvén velocity, v_A , the sound velocity, v_s , and the poloidal component of the velocity, v_p . In the magnetically driven region, the jet is accelerated to $v_p \geq 0.4c$, which is larger than Alfvén velocity. In the pressure-driven region, the gas pressure rather than the magnetic force is dominant, because the sound velocity is much larger than Alfvén velocity.

density increases, while the total velocity, v^{mag} decreases. The dependence of v_p^{mag} is the same as in the free-fall coronal cases, while that of v^{mag} is opposite. The later dependence of v^{mag} occurs because the rotational velocity, v_ϕ of the light disk increases more rapidly than that of the heavy disk, because of the more rapid fall of the lighter disk into the inner orbit with the faster Keplerian velocity.

The maximum poloidal component of the velocity of the magnetically driven jet increases as the initial magnetic field increases, $v_j \propto B^a$, where $a \sim 0.5$ – 0.8 (see cases M, J, and N), which is similar to the relation known for the magnetically driven steady jets (Kudoh & Shibata 1995, 1997a, 1997b). On the other hand, the velocity of the gas-pressure-driven jet has no monotonic dependence on the initial magnetic field. This is because in the case that the initial magnetic field is stronger, the disk loses the angular momentum more rapidly and falls toward the black hole faster. The gas pressure in the shock region of the falling disk is larger, and the

gas-pressure-driven jet becomes faster when the magnetic field is smaller than the critical value $B_c = 0.4(\rho_0 c^2)^{1/2}$. When the field is stronger than B_c , the magnetic dragging against the jet propagation (i.e., the deceleration $\mathbf{J} \times \mathbf{B}$ force) owing to highly deformed magnetic field lines decelerate the jet as seen in Fig. 10d.

6. SUMMARY AND DISCUSSION

We performed GRMHD simulations of jet formation from magnetized accretion disks around the nonrotating black holes. Our numerical results are summarized as follows:

1. We have developed the GRMHD code and tested it using several fundamental cases such as the steady state shock propagation and Keplerian motion in the steady state falling corona.

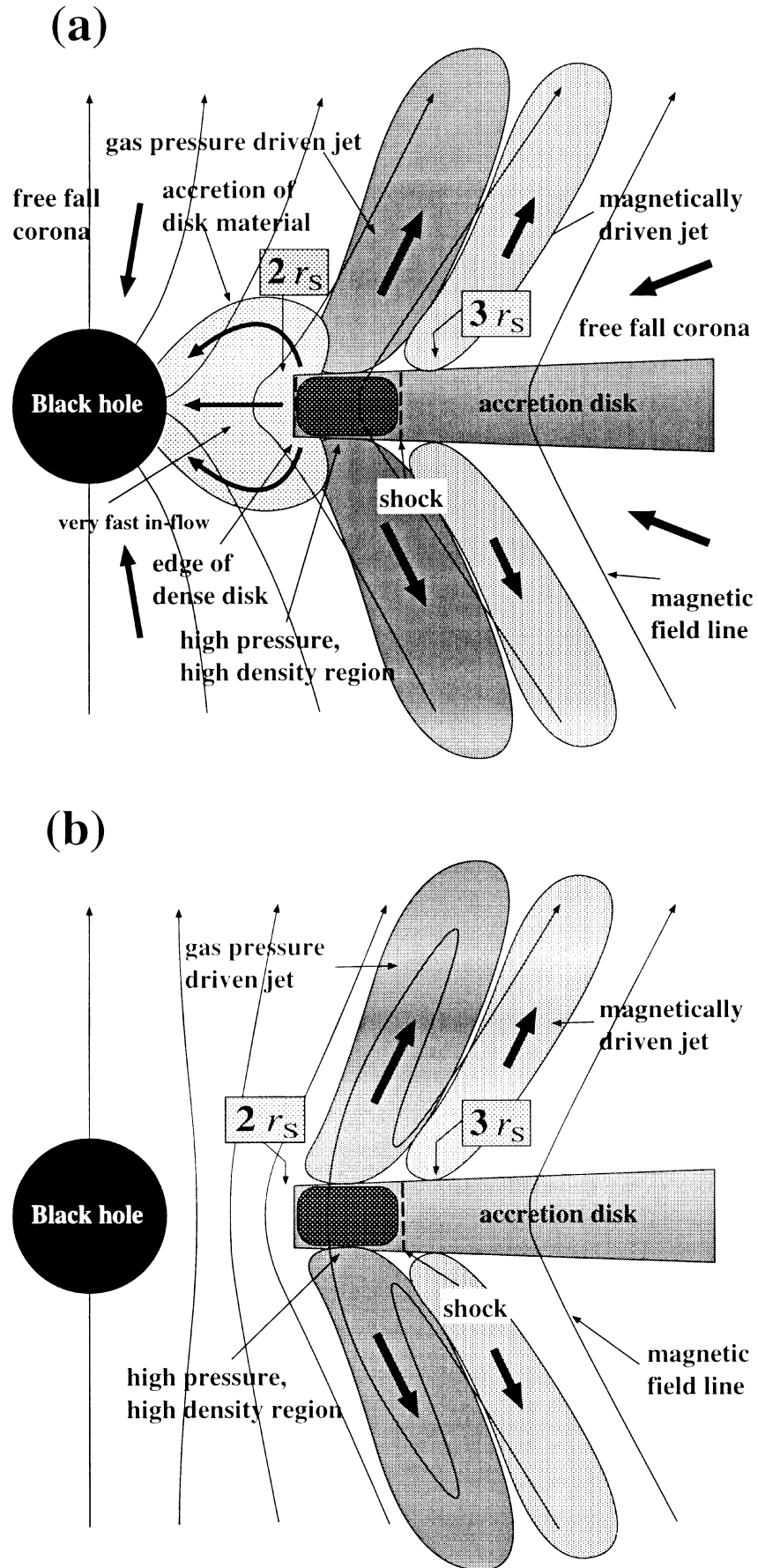


FIG. 15.—Schematic picture of two-layered shell structure of relativistic jet. (a) The transonic free-fall (steady state falling) corona case, and (b) the hydrostatic equilibrium coronal case.

First, we summarize the results of the jet formation in the steady state falling coronal cases.

2. When an accretion disk loses angular momentum by magnetic stress, the disk falls into the central object. However, it stops momentarily because of the centrifugal barrier when the specific angular momentum is greater than $2r_s c$, where we neglect the pressure effect. At the centrifugal barrier, the pressure and density increase drastically, accelerating the disk plasma in the z -direction.

3. When little or no magnetic field is applied, the plasma ejected from the disk falls into the black hole again.

4. When the magnetic field strength is strong enough, the ejection is collimated by the magnetic field and some parts become the fast jet owing to the combined acceleration from gas pressure and magnetic forces. We call this ejection the pressure-driven jet.

5. Outside of the pressure-driven jet, we found a region in which plasma is accelerated by magnetic forces alone, called the magnetically driven jet. That is, the whole jet has a two-layered shell structure, with the inner part accelerated by the high gas pressure and the outer part accelerated magnetically as in the nonrelativistic jet studied by Blandford & Payne (1983), Uchida & Shibata (1985), and Shibata & Uchida (1986). In the free-fall coronal cases, the magnetically driven jets are faster than the gas-pressure-driven jets. The maximum velocity of the jet is subrelativistic, $(0.3\text{--}0.4)c$ in all cases. Unfortunately, the simulations had to be stopped before they reached a stationary state, so we could not compare our numerical results with the steady state theory. The dependence of the jet velocity on the magnetic field strength is different from that of the theory.

6. As for the inner edge of the accretion disk, we emphasize that there is no real edge to the accretion disk material. However, the high pressure, dense region has an apparent edge near the foot of the pressure-driven jet caused by the watershed of the centrifugal barrier located at $(2\text{--}3)r_s$, for a nonrotating black hole. In fact, X-ray observations show that the inner edge is located at $r_D = (2.6 \pm 0.3)r_s$ (Bromley et al. 1998). This could be explained by a critical point located at $2r_s < r_D < 3r_s$.

Second, we summarize the results of the hydrostatic equilibrium coronal cases.

7. To compare the relativistic and nonrelativistic simulation of Shibata & Uchida (1986) directly, we perform the simulation with the hydrostatic corona. The structure of the formed jet is similar to that in the free-fall case. Namely, it has the two-layered shell structure, whose inner and outer parts are the gas pressure and magnetically driven jets, respectively. In this case, the gas-pressure-driven jet is much faster than the magnetically driven jet. The shock in the disk within the unstable orbit region is so strong that the pressure-driven jet is relativistic $v_j \sim 0.9c$, which is never seen in the nonrelativistic calculations of the thin-disk model. The outer part is the same as that in the nonrelativistic simulations by Shibata & Uchida (1986). The parameter survey shows that the dependence of the jet velocity on the magnetic field strength is consistent with the prediction of the steady state theory (Kudoh & Shibata 1995, 1997a).

We have discussed some explanations of these results in the previous sections (§§ 4 and 5). However, further studies are required to explain the results quantitatively. The relativistic theory should be developed to explain these results in more general framework.

Let us briefly discuss application of our results to AGNs. We examine the mass accretion rate \dot{M}_{ac} of the case A. The accretion rate is $\dot{M}_{ac} = 22\rho_0 r_s^2 c$. The characteristic mass of the central object in an AGN is estimated as $10^9 M_\odot$ (Malkan 1983). The typical mass density ρ_0 is estimated by

$$\rho_0 = 10^{17} m_H \dot{m} \alpha^{-1} M_8^{-1} (2r/r_s)^{-3/2} \text{ kg m}^{-3}, \quad (29)$$

where m_H , \dot{m} , α , and M_8 are the mass of the ion, the accretion rate normalized by Eddington rate, the flow viscosity parameter, and the mass of the black hole normalized by $10^8 M_\odot$, respectively (Rees 1984). When we assume $\dot{m} = 0.1$ and $\alpha = 0.2$, and $r = 3r_s$, it yields $\rho_0 = 1 \times 10^{-10} \text{ kg m}^{-3}$. We get the accretion rate from the simulation, $\dot{M}_{ac} = 50 M_\odot \text{ yr}^{-1}$. This is consistent with the observation $\dot{M}_{ac} = 10\text{--}50 M_\odot \text{ yr}^{-1}$, which is determined by the spectral model fitting (Malkan 1983).

Standard relativistic theory of the jet and wind formation (Camenzind 1986) states that even a relativistic jet will be accelerated gradually only by magnetic forces. However, our simulations show that rapid acceleration by gas pressure near the black hole is also important in relativistic jet formation. Furthermore, when the black hole rotates, as is recently indicated by line-emission observations (Bromley, Chen, & Miller 1997), the acceleration near the black hole (in an *ergosphere*) should become more important, as proposed by Cao (1997). A calculation using the Kerr metric, which describes the spacetime of a rotating black hole, will be performed in our future work (see Appendix C). It is also interesting to compare our calculation with the observations of the line emission from near the Schwarzschild stable-orbit limit (Tanaka et al. 1995). The evaluation will be performed in our future work.

In this paper, we report the basic method of our GRMHD simulation code, the test calculations and application of the code to the jet formation from an accretion disk around a nonrotating black hole. There are many other phenomena related with black holes and magnetic fields. For example, one of the most mysterious phenomena in astrophysics is γ -ray burst, which may be explained by the collision of the black hole and the strongly magnetized (neutron) star (Ramaprakash et al. 1998; Kulkarni et al. 1998). This is our future work.

One of authors (S. K.) thanks M. Inda-Koide for her discussion and important comments for this study. He also thanks D. L. Meier for useful discussions and hospitality during his visit at Jet Propulsion Laboratory. D. L. Meier and K.-I. Nishikawa spent considerable effort checking our manuscript. We appreciate their important comments and suggestions. We thank M. Takahashi, A. Tomimatsu, J. F. Hawley, T. Yokoyama, K. Hirotani, J.-I. Sakai, and R. L. Mutel for their discussions and encouragement. We appreciate the support of the National Institute for Fusion Science and the National Astronomical Observatory for the use of supercomputers.

APPENDIX A

FORMALISM OF GENERAL RELATIVISTIC MHD EQUATIONS

We present the 3 + 1 formalism of GRMHD time evolution equations derived from equations (1)–(3). We observe the vectors, such as velocity \mathbf{v} , magnetic field \mathbf{B} , and electric field \mathbf{E} in the fiducial coordinates,

$$v_i = ch_i U^i / \gamma, \quad (\text{A1})$$

$$B_i = \epsilon_{ijk} h_i F^{jk} / J, \quad (\text{A2})$$

$$E_i = F^{0i} / (h_0 h_i), \quad (\text{A3})$$

respectively, where the indices i, j , and k run from 1 to 3. Here Lorentz factor γ and Jacobian J are defined as $\gamma = 1/[1 - (v/c)^2]^{1/2}$ and $J = h_1 h_2 h_3$. We use the conservative quantities in the fiducial coordinates,

$$D = \gamma \rho, \quad (\text{A4})$$

$$\epsilon = (e + p)\gamma^2 - p - Dc^2 + \frac{B^2 + E^2/c^2}{2}, \quad (\text{A5})$$

$$\mathbf{P} = (e + p)\gamma^2 \mathbf{v}/c^2 + (\mathbf{E} \times \mathbf{B})/c^2, \quad (\text{A6})$$

and the stress tensor (opposite to the usual sign) $T^{ij} \equiv h_i h_j T_g^{ij}$, ($i, j = 1, 2, 3$),

$$T = p\mathbf{I} + \frac{(e + p)\gamma^2}{c^2} \mathbf{v}\mathbf{v} - \mathbf{B}\mathbf{B} - \frac{1}{c^2} \mathbf{E}\mathbf{E} + \left(\frac{B^2 + E^2/c^2}{2}\right)\mathbf{I}. \quad (\text{A7})$$

The magnetic field \mathbf{B} and the electric field \mathbf{E} are normalized as $\mathbf{B} = \mathbf{B}^*/\mu^{1/2}$ and $\mathbf{E} = \mathbf{E}^*/\mu^{1/2}$, respectively, where μ is the magnetic permeability and the quantity with an asterisk is in the MKSA unit system (SI unit). Using the normalized variables, equations (1)–(3) are written as the conservation forms,

$$\frac{\partial \mathbf{u}}{\partial t} = -q \circ \left[\frac{\partial}{\partial x^1} (h_0 \mathbf{b}_1 \circ \mathbf{w}_1) + \frac{\partial}{\partial x^2} (h_0 \mathbf{b}_2 \circ \mathbf{w}_2) + \frac{\partial}{\partial x^3} (h_0 \mathbf{b}_3 \circ \mathbf{w}_3) \right] + h_0 \mathbf{f}, \quad (\text{A8})$$

where \circ is defined as

$$\mathbf{a} \circ \mathbf{b} \equiv \begin{pmatrix} a_1 \\ \vdots \\ a_n \end{pmatrix} \circ \begin{pmatrix} b_1 \\ \vdots \\ b_n \end{pmatrix} \equiv \begin{pmatrix} a_1 b_1 \\ \vdots \\ a_n b_n \end{pmatrix}.$$

The time and the spatial derivative are clearly separated and these equations reduce to the classical MHD equations on the nonrelativistic limit. Hence we call these 3 + 1 formalism of the GRMHD equations. Here the matrices are defined as follows:

$$\mathbf{u} \equiv (D \quad P_1 \quad P_2 \quad P_3 \quad \epsilon \quad B_1 \quad B_2 \quad B_3)^T, \quad (\text{A9})$$

$$\mathbf{q} \equiv (1/J \quad 1/J \quad 1/J \quad 1/J \quad 1/J \quad h_1/J \quad h_2/J \quad h_3/J)^T, \quad (\text{A10})$$

$$(\mathbf{b}_1, \mathbf{b}_2, \mathbf{b}_3) \equiv \begin{pmatrix} h_2 h_3 & h_3 h_1 & h_1 h_2 \\ h_2 h_3 & h_3 h_1 & h_1 h_2 \\ h_2 h_3 & h_3 h_1 & h_1 h_2 \\ h_2 h_3 & h_3 h_1 & h_1 h_2 \\ h_2 h_3 & h_3 h_1 & h_1 h_2 \\ 0 & h_3 & h_2 \\ h_3 & 0 & h_1 \\ h_2 & h_1 & 0 \end{pmatrix}, \quad (\text{A11})$$

$$(\mathbf{w}_1, \mathbf{w}_2, \mathbf{w}_3) \equiv \begin{pmatrix} Dv_1 & Dv_2 & Dv_3 \\ T^{11} & T^{12} & T^{13} \\ T^{21} & T^{22} & T^{23} \\ T^{31} & T^{32} & T^{33} \\ c^2(P_1 - Dv_1) & c^2(P_2 - Dv_2) & c^2(P_3 - Dv_3) \\ 0 & E_3 & -E_2 \\ -E_3 & 0 & E_1 \\ E_2 & -E_1 & 0 \end{pmatrix}, \quad (\text{A12})$$

$$f \equiv \begin{pmatrix} 0 \\ (\epsilon + Dc^2)G_{01} + G_{12}T^{21} + G_{13}T^{31} - G_{21}T^{22} - G_{31}T^{33} \\ (\epsilon + Dc^2)G_{02} + G_{23}T^{32} + G_{21}T^{12} - G_{32}T^{33} - G_{12}T^{11} \\ (\epsilon + Dc^2)G_{03} + G_{31}T^{13} + G_{32}T^{23} - G_{13}T^{11} - G_{23}T^{22} \\ c^2(G_{01}P_1 + G_{02}P_2 + G_{03}P_3) \\ 0 \\ 0 \\ 0 \end{pmatrix}. \quad (\text{A13})$$

The curvature of the spacetime is described by

$$G_{\mu\nu} = -(h_\mu h_\nu)^{-1}(\partial h_\mu / \partial x^\nu). \quad (\text{A14})$$

Furthermore, the frozen-in condition of equation (8) becomes

$$\mathbf{E} = -\mathbf{v} \times \mathbf{B}, \quad (\text{A15})$$

which is identical to the Newtonian case. The electric charge conservation law is yielded from equation (4),

$$\frac{\partial \rho_c}{\partial t} + \frac{h_0}{J} \sum_i \frac{\partial}{\partial x^i} \left(\frac{J}{h_i} J_i \right) = 0, \quad (\text{A16})$$

$$\rho_c = \frac{1}{c^2} \frac{h_0}{J} \sum_i \frac{\partial}{\partial x^i} \left(\frac{J}{h_i} E_i \right), \quad (\text{A17})$$

where $\rho_c = h_0^2 J^0$, $J_i = h_0 h_i J^i$ ($i = 1, 2, 3$) with four current density (J^0, J^1, J^2, J^3). The current density is explicitly written by

$$J_i = \sum_{jk} \frac{h_i}{h_1 h_2 h_3} \epsilon_{ijk} \frac{\partial}{\partial x^j} (h_0 h_k B_k) - \frac{1}{c^2} \frac{\partial E_i}{\partial t}. \quad (\text{A18})$$

The electric charge density ρ_c and the electric current density \mathbf{J} are normalized as $\rho_c = \mu^{1/2} \rho_c^*$ and $\mathbf{J} = \mu^{1/2} \mathbf{J}^*$, respectively.

The first component of equation (A8) gives the mass conservation equation. The second, third, and fourth components present the equation of motion. The fifth one is about the energy conservation law, and components from sixth to eighth component express Faraday's law.

In the case of $h_0 = 1$, these equations reduce to the special relativistic equations with the general coordinates formally. One needs only add the gravitational term and factor h_0 into the special relativistic code to develop the GRMHD code from the special relativistic one. The reader may find that it is easy to develop the code. The following procedure is recommended for developing the reader's GRMHD code.

1. Begin with making of the Newtonian MHD code on (three-dimensional) Cartesian coordinates by the Lax-Wendroff or TVD scheme, etc.
2. Modify the code to a special relativistic one. Here one may use the Newton-Raphson method to solve equations (9) and (10).
3. Modify the code to a special relativistic one with general coordinates. One may check the code by some simple problems in cylindrical coordinates, for example nonrelativistic Keplerian motion.
4. Modify the code to a general relativistic one. Here one just adds the gravitational term and the factor h_0 to the previous version according to the equations in this Appendix. This modification is easy and takes less than 1 hr. Then one gets a (three-dimensional) GRMHD code!

Here procedures (2) and (3) are interchangeable. This GRMHD code treats only nonrotating black holes. Using the method described in Appendix C, one can extend the application of a GRMHD code to rotating black holes.

APPENDIX B

RELATIVISTIC EXPRESSIONS OF POWER

We derive the expression of the power evaluation from the pressure and electromagnetic forces to the motion of the (jet) material. We consider the power in the fiducial observer, and hence we use the special relativistic framework. In the special relativistic framework, the equation of motion is

$$\frac{\partial}{\partial t} \left(\frac{\gamma^2 h}{c^2} \mathbf{v} + \frac{1}{c^2} \mathbf{E} \times \mathbf{B} \right) = -\nabla \cdot \left[\frac{\gamma^2 h}{c^2} \mathbf{v} \mathbf{v} + p \mathbf{I} - \mathbf{B} \mathbf{B} + \frac{B^2}{2} \mathbf{I} + \frac{1}{c^2} \left(-\mathbf{E} \mathbf{E} + \frac{E^2}{2} \mathbf{I} \right) \right]. \quad (\text{B1})$$

The Maxwell equations are

$$\frac{\partial \mathbf{B}}{\partial t} = -\nabla \times \mathbf{E}, \quad (\text{B2})$$

$$\frac{1}{c^2} \frac{\partial \mathbf{E}}{\partial t} + \mathbf{J} = \nabla \times \mathbf{B}, \quad (\text{B3})$$

$$\frac{1}{c^2} \nabla \cdot \mathbf{E} = \rho_c, \quad (\text{B4})$$

$$\nabla \cdot \mathbf{B} = 0. \quad (\text{B5})$$

Using the Maxwell equations, we have

$$\nabla \cdot \left[\mathbf{B}\mathbf{B} - \frac{B^2}{2} \mathbf{I} + \frac{1}{c^2} \left(\mathbf{E}\mathbf{E} - \frac{E^2}{2} \mathbf{I} \right) \right] = \rho_c \mathbf{E} + \mathbf{J} \times \mathbf{B} + \frac{\partial}{\partial t} \left(\frac{1}{c^2} \mathbf{E} \times \mathbf{B} \right).$$

Then the equation of motion yields

$$\frac{\partial}{\partial t} (R\mathbf{v}) + \nabla \cdot (R\mathbf{v}\mathbf{v}) = -\nabla p + \rho_c \mathbf{E} + \mathbf{J} \times \mathbf{B}, \quad (\text{B6})$$

where $R \equiv \gamma^2 h/c^2$. In the case of the nonrelativistic limit, this equation is reduced to the Newtonian equation of motion. However, unfortunately, we cannot get an expression that corresponds to the kinetic energy equation in Newtonian mechanics. Instead of that equation, we derive a similar conservation equation. Making a direct product of \mathbf{v}/v and the equation of motion, we get,

$$\frac{\partial}{\partial t} (Rv) + \nabla \cdot (Rv\mathbf{v}) = \frac{\mathbf{v}}{v} \cdot (-\nabla p + \rho_c \mathbf{E} + \mathbf{J} \times \mathbf{B}). \quad (\text{B7})$$

This equation is also written as

$$\frac{\partial}{\partial t} \left(\frac{R}{2} v^2 \right) + \nabla \cdot \left(\frac{R}{2} v^2 \mathbf{v} \right) + \frac{v^2}{2} \left[\frac{\partial R}{\partial t} + \nabla \cdot (R\mathbf{v}) \right] = \mathbf{v} \cdot (-\nabla p + \rho_c \mathbf{E} + \mathbf{J} \times \mathbf{B}). \quad (\text{B8})$$

This later equation clearly is reduced to the Newtonian equation of the kinetic energy when we take the nonrelativistic limit ($p \ll \rho c^2$, $v \ll c$) and the conservation of mass density $\partial \rho / \partial t + \nabla \cdot (\rho \mathbf{v}) = 0$. However, this equation is not of the conservation type, and hence we cannot take the $Rv^2/2$ as the relativistic kinetic energy. We use the former conservation-type equation (B7) to evaluate the power of the pressure and electromagnetic forces to the fluid motion. Then to evaluate the power contribution, we use

$$S = S_{\text{pg}} + S_{\text{EM}}$$

$$S_{\text{pg}} \equiv \frac{\mathbf{v}}{v} \cdot (-\nabla p)$$

$$S_{\text{EM}} \equiv \frac{\mathbf{v}}{v} \cdot (\rho_c \mathbf{E} + \mathbf{J} \times \mathbf{B}),$$

where S_{pg} and S_{EM} are the contributions from the gas pressure and the electromagnetic force, respectively. To compare just the value of the gas pressure and the electromagnetic force contributions at a fixed point, we can use the familiar powers $W_{\text{pg}} \equiv -\mathbf{v} \cdot \nabla p$ and $W_{\text{EM}} \equiv \mathbf{v} \cdot (\rho_c \mathbf{E} + \mathbf{J} \times \mathbf{B})$, respectively. In the ideal MHD assumption, $\mathbf{E} + \mathbf{v} \times \mathbf{B} = 0$, we can write $W_{\text{EM}} \equiv \mathbf{v} \cdot (\mathbf{J} \times \mathbf{B})$ because of $\mathbf{v} \cdot (\rho_c \mathbf{E}) = 0$.

APPENDIX C

THE CALCULATION WITH KERR METRIC

Here we introduce a method for extending the code to the case of a rotating black hole, that is, a Kerr black hole. On the normalization $c = 1$ and $G = 1$, the Kerr metric on the Boyer-Lindquist coordinates $(x^0, x^1, x^2, x^3) = (t, r, \theta, \phi)$ is written as

$$ds^2 = -h_0^2(dt)^2 - \sum_i 2h_i \Omega_i dx^i dt + \sum_i h_i^2(dx^i)^2, \quad (\text{C1})$$

where

$$h_0^2 = 1 - \frac{2mr}{\Sigma}, \quad h_1^2 = \frac{\Sigma}{\Delta}, \quad h_2^2 = \Sigma, \quad h_3^2 = \frac{A}{\Sigma} \sin^2 \theta,$$

$$\frac{\Omega_3}{h_3} = \frac{2mar}{A}, \quad \Omega_1 = \Omega_2 = 0,$$

$$\Delta \equiv r^2 - 2mr + a^2, \quad \Sigma \equiv r^2 + a^2 \cos^2 \theta,$$

$$A \equiv (r^2 + a^2)^2 - \Delta a^2 \sin^2 \theta.$$

Here m and a are the mass and the angular momentum per unit mass of the black hole. Note that $\Delta = 0$ gives the event horizon $r = r_H$ and $h_0 = 0$ is static limit surface $r = r_0$ (Takahashi et al. 1990). To perform calculations with the Kerr metric, we should modify the present GRMHD code as follows. Here we describe only the main procedure for developing a Kerr GRMHD code. Details will be reported in a following paper.

1. We use the conservation quantities in the corotating frame (CRF) around a Kerr black hole. The expressions of the conservation quantities and stress tensor (A4)–(A7) do not change when we modify the definitions of the velocity v_i , electric field E_i and four energy-momentum tensor $T^{\alpha\beta}$:

$$v_i = \frac{h_i}{\gamma} U^i - \frac{\Omega_i}{h'_0}, \quad (C2)$$

$$E^i = \frac{F_{i0}}{h_i h'_0} + \sum_j \frac{\Omega_j}{h'_0 h_i h_j} F_{ij}, \quad (C3)$$

$$T^{\alpha\beta} = h'_\alpha h'_\beta T_g^{\alpha\beta} - \Omega_\beta h'_\alpha T_g^{\alpha 0} - \Omega_\alpha h'_\beta T_g^{\beta 0} + \Omega_\alpha \Omega_\beta T_g^{00}, \quad (C4)$$

where indices i and j run from 1 to 3 and α and β run from 0 to 3, $\gamma = h'_0 U^0$, $h'_0 = (h_0^2 + \Omega_1^2 + \Omega_2^2 + \Omega_3^2)^{1/2}$, $h'_i = h_i$, $\Omega_0 = 0$, and $\Omega_i = \Omega_i$. Other quantities, for example, the scalar quantities and magnetic field, don not change in form. Therefore the algebraic equations (9) and (10) are also used even in Kerr black hole calculation. We also use variables in the locally nonrotating frame (LNRF) with a tilde, which are the same in form as those of the Schwarzschild metric case, for example, $\tilde{T}^{\alpha\beta} = h'_\alpha h'_\beta T_g^{\alpha\beta}$ and $\tilde{F}_{\alpha\beta} = F_{\alpha\beta}/(h'_\alpha h'_\beta)$.

2. The left-hand side of the time evolution equation (A8) does not change.

3. The quantities in the right-hand side of equation (A8) should be replaced by those in the LNRF. We must also modify h_0 to h'_0 . The above procedure completes the equations of mass conservation and Faraday's law for the calculation in Kerr metric.

4. Concerning to the equation of motion, the tensor \tilde{T}^{ij} in the spatial derivative should be replaced by $\tilde{T}^{ij} - \Omega_i \tilde{T}^{0j}/h'_0$. We also add the new source term

$$s'_i = - \frac{\Omega_1^2 + \Omega_2^2 + \Omega_3^2}{h'_0} G_{0i} \tilde{T}^{00} - \sum_j \left(\Omega_i G_{ij} + \frac{1}{h_i h_j} \frac{\partial h_j \Omega_j}{\partial x^i} \right) \tilde{T}^{0j}.$$

5. We have to add the new source term

$$s'_0 = - \sum_i \left(\frac{\Omega_1^2 + \Omega_2^2 + \Omega_3^2}{h'_0} G_{0i} \tilde{T}^{0i} + \frac{\Omega_i s'_i}{h'_0} \right) - \sum_{ij} \frac{1}{h_j} \frac{\partial \Omega_i}{\partial x^j} \tilde{T}^{ij},$$

to the energy equation.

To avoid the apparent singularity in the ergosphere, it is better to use $G'_{0i} \equiv (h_0/h'_0)^2 G_{0i}$ instead of G_{0i} . Then one obtains the relativistic MHD code with Kerr metric. Note that the divergence-free condition of the magnetic field does not change, while the electric source free condition should be modified.

APPENDIX D

SIMPLIFIED TOTAL VARIATION DIMINISHING METHOD

Here we briefly explain the simplified total variation diminishing (TVD) method. We consider a conservation equation $\partial u(x, t)/\partial t = -\partial w(u, x)/\partial x$ in one dimension, where u and w are the m -dimension vector in general. The procedure of the

simplified TVD scheme is as follows (Davis 1984):

$$\begin{aligned} u_j^{(1)} &= u_j^n - \kappa(w_j^n - w_{j-1}^n), \\ u_j^{(2)} &= \frac{1}{2} [u_j^n + u_j^{(1)} - \kappa(w_{j+1}^{(1)} - w_j^{(1)})], \\ u_j^{n+1} &= u_j^{(2)} + D_{j+1/2}^n - D_{j-1/2}^n, \end{aligned} \quad (D1)$$

where $\kappa \equiv \Delta t / \Delta x$, the superscript n denotes the time step, and the subscript j indicates the mesh point. Here the last terms, $D_{j+1/2}^n$, are defined as follows,

$$\begin{aligned} D_{j+1/2}^n &= [\bar{K}^+(v, r_j^+) + \bar{K}^-(v, r_{j+1}^-)](u_{j+1}^n - u_j^n), \\ v &= \max_m (|c_m|) \kappa, \end{aligned} \quad (D2)$$

$$\bar{K}^\pm(v, r^\pm) = 0.5C(v)[1 - \phi(r^\pm)],$$

$$\phi(r) = \begin{cases} \min\{2r, 1\} & \text{for } r > 0, \\ 0 & \text{for } r \leq 0, \end{cases}$$

$$C(v) = \begin{cases} v(1-v) & \text{for } v \leq 0.5, \\ 0.25 & \text{for } v > 0.5, \end{cases}$$

$$r_j^+ = \frac{(\Delta u_{j-1/2}^n, \Delta u_{j+1/2}^n)}{(\Delta u_{j+1/2}^n, \Delta u_{j+1/2}^n)},$$

$$r_j^- = \frac{(\Delta u_{j-1/2}^n, \Delta u_{j+1/2}^n)}{(\Delta u_{j-1/2}^n, \Delta u_{j-1/2}^n)},$$

$$\Delta u_{j+1/2}^n = u_{j+1}^n - u_j^n,$$

and c_j is the speed of each wave, and the parentheses denote the usual inner product on \mathbf{R}^m . This scheme is regarded as Lax-Wendroff's scheme with an additional diffusion term. When we extend this scheme into a two-dimensional one by means of the splitting method, a weak checkerboard numerical instability appears. To avoid this instability, we combine the two coefficients \bar{K}^+ and \bar{K}^- into a single coefficient \bar{K} defined as

$$\bar{K}(v, r^+, r^-) = 0.5C(v)[1 - \phi(r^+, r^-)], \quad (D3)$$

$$\phi(r^+, r^-) = \max [0, \min (2r^+, r^-, 1), \min (2r^-, r^+, 1)].$$

REFERENCES

- Bell, A. R., & Lucek, S. G. 1995, MNRAS, 277, 1327
 Begelman, M. C., & Li, Z.-Y. 1994, ApJ, 426, 269
 Beskin, V. S. 1997, Phys. Uspekhi, 40, 659
 Blandford, R. D., & Payne, D. G. 1982, MNRAS, 199, 883
 Bondi, H., & Hoyle, F. 1944, MNRAS, 104, 273
 Bromley, B. C., Chen, K., & Miller, W. 1997, ApJ, 475, 57
 Bromley, B. C., Miller, W. A., & Pariev, V. I. 1998, Nature, 391, 54
 Camenzind, M. 1986, A&A, 156, 137
 Cao, X. 1997, MNRAS, 291, 145
 Davis, S. F. 1984, NASA Contractor Rep. 172373 (ICASE Rep. 84-20) (Washington: NASA)
 Duncan, G. C., & Hughes, P. A. 1994, ApJ, 436, L119
 Eikenberry, S. S., Matthews, K., Morgan, E. H., Remillard, R. A., & Nelson, R. W. 1998, ApJ, 494, L61
 Hawley, J. F., & Smarr, L. L. 1985, in AIP Conf. Proc. 144, Magnetospheric Phenomena in Astrophysics, ed. R. I. Epstein & W. C. Feldman (New York: AIP), 263
 Hughes, P. A. 1991, Beams and Jets in Astrophysics (New York: Cambridge Univ. Press)
 Khanna, R. 1998, MNRAS, 294, 673
 Koide, S. 1997, ApJ, 478, 66
 Koide, S., Nishikawa, K.-I., & Mutel, R. L. 1996, ApJ, 463, L71
 Koide, S., Shibata, K., & Kudoh, T. 1998, ApJ, 495, L63
 Kudoh, T. 1994, MNRAS, 266, 609
 Kudoh, T., & Kaburaki, O. 1996, ApJ, 460, 199
 Kudoh, T., Matsumoto, R., & Shibata, K. 1998, ApJ, 508, 186
 Kudoh, T., & Shibata, K. 1995, ApJ, 452, L41
 ———. 1997a, ApJ, 476, 632
 ———. 1997b, ApJ, 474, 362
 Kulkarni, S. R., et al. 1998, Nature, 393, 35
 Li, Z.-Y., Chiueh, T., & Begelman, M. C. 1992, ApJ, 394, 459
 Lovelace, R. V. E. 1976, Nature, 262, 649
 Lynden-Bell, D. 1969, Nature, 223, 690
 Malkan, M. A. 1983, ApJ, 268, 582
 Matsumoto, R., Uchida, Y., Hirose, S., Shibata, K., Hayashi, M. R., Ferrari, A., Bodo, G., & Norman, C. 1996, ApJ, 461, 115
 Meier, D. L., Edgington, S., Godon, P., Payne, D. G., & Lind, K. R. 1997, Nature, 388, 350
 Mirabel, I. F., & Rodriguez, L. F. 1994, Nature, 371, 46
 Miyoshi, M., Moran, J., Hernstein, J., Greenhill, L., Nakai, N., Diamond, P., & Inoue, M. 1995, Nature, 373, 127
 Molteni, D., Lanzafame, G., & Chakrabarti, S. K. 1994, ApJ, 425, 161
 Nishikawa, K.-I., Koide, S., Sakai, J.-I., Christodoulou, D. M., Sol, H., & Mutel, R. L. 1997, ApJ, 483, L45
 ———. 1998, ApJ, 498, 166
 Okamoto, I. 1992, MNRAS, 254, 192
 Ouyed, R., Pudritz, R. E., & Stone, J. M. 1997, Nature 385, 409
 Pearson, J. J., et al. 1981, Nature, 290, 365

- Pelletier, G., Ferreira, J., Henri, G., & Marcowith, A. 1996, in *Solar and Astrophysical Magnetohydrodynamic Flows*, ed. K. C. Tsinganos (Dordrecht: Kluwer), 643
- Pudritz, R. E., & Norman, C. 1986, *ApJ*, 301, 571
- Ramaprakash, A. N., et al. 1998, *Nature*, 393, 43
- Rees, M. J. 1966, *Nature*, 211, 468
- . 1984, *ARA&A*, 22, 471
- Shibata, K., & Uchida, Y. 1986, *PASJ*, 38, 631
- Takahashi, M., Nitta, S., Tatematsu, Y., & Tomimatsu, A. 1990, *ApJ*, 363, 206
- Takahashi, M., & Shibata, S. 1998, *PASJ*, 50, 271
- Tanaka, Y., et al. 1995, *Nature*, 352, 659
- Thorne, K. S., Price, R. H., & Macdonald, D. A. 1986, *Membrane Paradigm* (New Haven: Yale Univ. Press)
- Tingay, S. J., et al. 1995, *Nature*, 374, 141
- Tomimatsu, A. 1994, *PASJ*, 46, 123
- Uchida, Y., & Shibata, K. 1985, *PASJ*, 37, 515
- van Putten, M. H. P. M. 1996, *ApJ*, 467, L57
- Wald, R. M. 1974, *Phys. Rev. D*, 10, 1680
- Weinberg, S. 1972, *Gravitation and Cosmology* (New York: Wiley)
- Yokosawa, M. 1993, *PASJ*, 45, 207